REPORT DOCUMENTATION PAGE

Form Approved
OMB No. 0704-0188

1. REPORT DATE (DD-MM-YYYY)	2. REPORT TYPE	3. DATES COVERED (From – To)
	Final Technical Report	1February 2004 – 31 December 2006

4. TITLE AND SUBTITLE
Direct Numerical Simulation of the Influence of Plasmas on Turbulent Flows

5a. CONTRACT NUMBER

5b. GRANT NUMBER
FA9550-04-1-0064

5c. PROGRAM ELEMENT NUMBER

6. AUTHOR(S)
Dr. Krishnan Mahesh

5d. PROJECT NUMBER

5e. TASK NUMBER

5f. WORK UNIT NUMBER

7. PERFORMING ORGANIZATION NAME(S) AND ADDRESS(ES
Aerospace Engineering and Mechanics
University of Minnesota MN   55455

8. PERFORMING ORGANIZATION REPORT NUMBER

9. SPONSORING/MONITORING AGENCY NAME(S) AND ADDRESS(ES)
Air Force Office of Scientific Research (AFOSR)
875 N. Arlington St., Rm. 3112
Arlington, VA 22203
Rhett Jeffries/NA

10. SPONSOR/MONITOR'S ACRONYM(S)
AFOSR

11. SPONSORING/MONITORING AGENCY REPORT NUMBER
N/A

12. DISTRIBUTION AVAILABILITY STATEMENT

DISTRIBUTION A: Approved for public release. Distribution is unlimited.

AFRL-SR-AR-TR-07-0209

13. SUPPLEMENTARY NOTES

14. ABSTRACT
This work uses direct numerical simulation to study the thermal effect of a region of plasma on quiescent air. The simulations solve the compressible ideal gas Navier-Stokes equations using Fourier spectral methods. A shock capturing scheme is incorporated to account for the strong shock waves. Also, a logarithmic formulation for the continuity equation is developed to handle low densities at the core of the plasma.

15. SUBJECT TERMS

16. SECURITY CLASSIFICATION OF:			17. LIMITATION OF ABSTRACT	18. NUMBER OF PAGES	19a. NAME OF RESPONSIBLE PERSON
a. REPORT	b. ABSTRACT	c. THIS PAGE	Unclassified	48	19b. TELEPONE NUMBER (Include area code)
Unclassified	Unclassified	Unclassified			(703)

Standard Form 298 (Rev. 8-98)
Prescribed by ANSI Std Z39-18

DIRECT NUMERICAL SIMULATION OF THE INFLUENCE OF PLASMAS ON TURBULENT FLOWS

1

1 Introduction

Plasmas have the potential to be used for the control and manipulation of diverse flow related applications. Most current works have considered the prospect of using plasmas for flow control by directly affecting the mean flow. This project is studying the ability of plasmas to directly influence the turbulent fluctuations in the interior of flows. Laser energy deposition has been considered to be the mode of plasma generation.

Laser energy deposition has been studied in great detail (e.g. Maker et al. 1963, Damon & Tomlinson 1963, Meyerand & Haught 1963). Applications of laser–induced breakdown of a gas include localized flow control of supersonic flows (Adelgren et al 2003), drag reduction in supersonic and hypersonic flows (Riggins 1999), ignition of combustion gases (Phuoc 2000) and providing thrust to aerospace vehicles (Molina-Morales et al 2001, Wang et al 2001).

When a laser beam is focused on a small volume of gas, the gas molecules in the focal volume absorb energy and get ionized. The laser beam can convert an optically transparent, gaseous region into opaque, highly conducting plasma, in a few nano–seconds. The plasma formation process involves multiple steps. The initial release of electrons is due to multi–photon ionization, which requires that multiple photons are incident on an atom simultaneously. Multiple photons are needed since ionization energies for most gases are larger than the energy of a single photon in the laser beam. During this process, the electron number density increases linearly in time. The released electrons in the focal volume absorb laser energy due to inverse bremsstrahlung absorption, where a free electron in presence of a third body, absorbs energy and gets excited. Many such interactions are needed for the electron to gain sufficient energy to impact ionize neutral atoms. The resultant electron concentration increases exponentially in time.

The plasma thus formed, absorbs laser energy and spreads out in the direction of the laser beam due to a combination of absorption and reflection. The highly ionized plasma in the focal volume reflects part of the laser energy incident on it. This energy is absorbed by adjacent molecules, in the direction of the laser beam. These molecules get ionized, and start reflecting laser radiation. This process continues until the plasma has spread out and assumed a tear–drop shape. The energized electrons collide with the heavy particles leading to heating of the gas. Also due to these collisions, the electrons get de–energized and recombine with ions, sharply decreasing the electron number density. Thus an energy spot with temperature and pressure higher than that of the surroundings is left at the end of the plasma formation process. The sharp pressure gradients lead to formation of a blast wave that propagates into the background gas.

Recent experimental work on pulsed laser induced breakdown in quiescent air or nitrogen, include Jiang et al. (1998), Lewis et al. (1999), Adelgren et al. (2001) and Yan et al. (2003). Jiang et al. (1998) used a laser beam of 1.38 J focused on a 3 mm diameter spherical region to cause breakdown in air. The laser was pulsed for a duration of 18 nanoseconds. Adelgren et al. (2001) used a Nd:YAG laser of 200 mJ pulsed for 10 nanosecond duration in air. Yan et al. (2003)
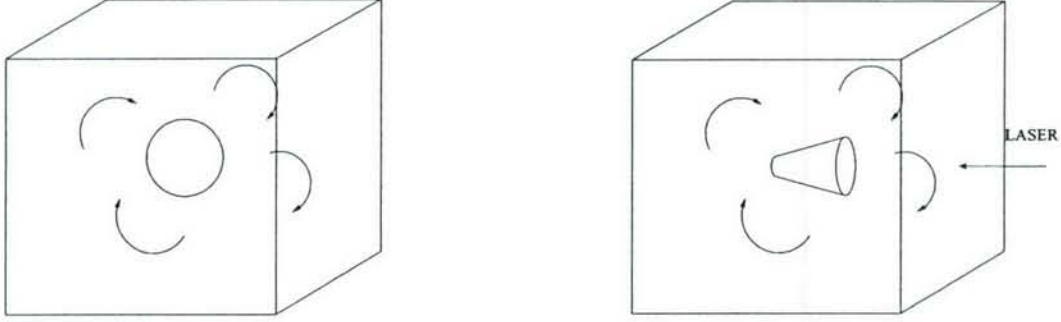
Figure 1: Schematic illustrating the thermal interaction between isotropic turbulence and spherical and conical idealizations of a region of plasma.

used a 108 – 145 mJ Nd:YAG laser pulsed for a duration of 10 nanoseconds over a focal volume of 3 mm^3 to induce breakdown in air. The experimental data show a wide separation in time–scales between the laser pulse duration and observations of the blast wave propagation. As seen above, the laser is pulsed on a time–scale of 10 nanoseconds. The blast wave, on the other hand is observed on a time–scale of 10 to 100 microseconds. Since plasma formation is on a time–scale of the same order as the laser pulse duration, the three to four order of magnitude separation in time–scale suggests that the plasma may be considered to be formed instantaneously to a first approximation, to evaluate its gas–dynamic effect on the surrounding fluid.

Various theoretical models have been used to understand different features of this phenomenon. Similarity laws proposed by Taylor (1950), Sedov (1959) and Von Neumann (1963) for the radius and speed of the blast wave produced from a point source apply to the early stages of the blast wave, when it is strong. Note however that at early stages, the blast wave need not be spherical, which reduces applicability of the classical analysis. Brode (1955) performed a numerical simulation of the blast wave and concluded that the ideal gas assumption was reasonable for shock pressures less than 10 atmospheres in air. Steiner et al. (1998) perform computations using a real gas model to show that, when initialized with a self similar strong shock solution, the shock radius in the real gas model is quite close to that predicted by the classical point source explosion in an ideal gas. Other computations of blast wave propagation in quiescent air include those by Jiang et al (1998) and Yan et al. (2003). Dors et al. (2000) present a computational model which considers the asymmetry of laser energy deposition as well as ionization and dissociation effects on fluid properties. The initial stages of plasma formation due to laser energy deposition were modeled by Kandala and Candler (2002).

This work considers generation of laser induced plasma in quiescent air and in background isotropic turbulence. A schematic for the problem is shown in figure

3

1. Local thermodynamic equilibrium conditions are assumed to apply. Only the thermal effects of the plasma are considered. Two types of idealizations have been used in the simulations to represent the initial shape of the plasma – spherical and tear–drop shaped. The spherical idealization corresponds to a point plasma region and is a good approximation only if the size of the plasma is small compared to other length–scales in the flow. The tear–drop shaped idealization on the other hand resembles the initial shape of the plasma observed in experiments of laser induced break down of a gas.

A Fourier spectral solver was developed for the simulations. The solver assumes periodic boundary conditions. If the plasma is assumed to be spherical in nature, then the flow would vary radially and in time. If the plasma is assumed to be tear–drop shaped, the flow would be axisymmetric and non–stationary in time. For both cases, the periodic boundary conditions would work fine as long as the blast wave does not touch the domain boundaries. This is because if the blast wave is well resolved, the gradients ahead of it will be zero.

This grant was used to support the doctoral research of Mr. Shankar Ghosh. Publications associated with this work are listed below.

- Direct numerical simulation of the thermal effects of plasmas on turbulent flows (AIAA Paper 2005-0407).

- Direct Numerical Simulation of the thermal effects in plasma/turbulence interaction (AIAA Paper 2007-993).

- DNS of the thermal effects of laser energy deposition in a fluid at rest (submitted to Journal of Fluid Mechanics).

- Numerical issues associated with simulation of strong blast waves in high temperature flows interacting with a turbulent background (under preparation for submission to the Journal of Computational Physics).

The principal contributions of this work are listed below.

- A parallel compressible Navier–Stokes solver has been developed. The solver uses Fourier spectral spatial derivatives. Skew symmetric form of the non–linear terms are used to suppress aliasing error. A fourth order Runge-Kutta scheme has been used for time advancement.

- A pencil data structure has been used to parallelize the solver. An efficient algorithm has been implemented to compute transposes for data along the y and z directions. The solver has been ported and tested on different platforms (Sdsc Teragrid, Datastar, Bluegene), the largest simulation so far being a 512 cube simulation on 1024 processors.

- A predictor–corrector based shock capturing scheme has been implemented to capture strong shock waves observed in the simulations. The scheme (Yee et al 1999) has a finite volume based formulation and has been applied as a corrector step to the spectral base numerical scheme.

4

- Shock capturing needs to be implemented without excessively dissipating the turbulence in the background. This is achieved by developing a non-linear switch that detects the shock wave and applies shock capturing only to its vicinity.

- Since the simulations involve very high temperatures, the finite volume formulation of the shock capturing scheme needs to be extended suitably for high temperatures. A formal derivation of the Jacobian matrix, eigen values and eigen vector matrices has been derived for a generalized geometry (Appendix).

- There is significant expansion in the plasma core leading to very low densities there. Slight oscillations can thus lead to densities becoming negative rendering the solution unstable. To avoid this a logarithm formulation of the continuity equation has been used to ensure that density remains positive even in regions of very low density.

- Based on the amount of energy deposited in the flow, the blast wave reaches the domain boundaries on a certain time scale. To study further evolution of the plasma core the domain boundaries need to be expanded. This is done by interpolating the solution form a smaller to a larger domain using a spectral interpolation scheme.

- In the case of spherical energy deposition, the post energy deposition process can be divided into two parts – shock formation and shock propagation. These phases have been described based on conversion of internal energy of the core into kinetic energy of surrounding fluid elements and generation of sharp pressure gradients in the flow.

- The shock radius evolution in time has been compared to the strong shock solution (Taylor 1950, Sedov 1959) and found to compare well at short times and deviate towards the acoustic limit at longer times. Lesser the energy deposited in the flow, sooner is the deviation towards the acoustic limit. Similar analysis is also presented for velocity at the shock front.

- A reverse flow is observed behind the shock front at later times. Existence of this reverse flow is explained based on conservation of mass behind the shock front. The reverse flow is observed to be symmetric in nature.

- In the case of the tear–drop shaped plasma, shock radius evolution in time and jumps in flow variables at the shock front are compared with data obtained from experiments conducted by Adelgren (2001) and simulations conducted by Kandala and Candler (2003).

- Again post energy deposition is divided into formation and propagation of a blast wave. However the blast wave is initially asymmetrical tear–drop shaped as characterized by sharp pressure gradients normal to the plasma axis. This blast wave propagates into the background becoming spherical in time.

5

- Baroclinic vorticity is found to be generated near the leading and trailing edges of the plasma at short times. This is explained based on a relation suggested by Truesdell (1952).

- Budgets have been computed for the vorticity transport equation. They indicate that vorticity generated by baroclinic means is convected radially outward and suppressed by bulk expansion behind the blast wave.

- For longer times an asymmetric reverse flow is observed behind the shock front resulting in the rolling up of the flow field. This leads to advection of the temperature profile such that the maximum temperature shifts away from the plasma axis. This is in good agreement with experimental observation of the resulting flow field.

- The resulting vorticity field is observed to be much more complicated than a simple toroidal vortex ring observed in the experiments. However the vorticity magnitude is observed to be much larger for the rings closest to the plasma axis and so these are the ones that are observed in the experiments.

- In the case of the spherical plasma interacting with background turbulence, a spherically symmetric blast wave is observed to propagate through the background turbulence. Turbulence levels are observed to get amplified across the blast wave. Amplification is most pronounced in the radial component of velocity and the transverse component of vorticity.

- In the case of the tear–drop shaped plasma interacting with background turbulence, a tear–drop shaped blast wave is observed to propagate through the background turbulence becoming more and more spherical in time.

- The blast wave strongly compresses the background turbulence. Significant expansion is observed in the turbulent core.

- The blast wave is initially very strong and is not distorted by the background turbulence. However, as it propagates into the background, the effect of the turbulence is to dampen its intensity and soon it becomes weak enough to get distorted through interaction with the turbulence.

- Statistics computed for turbulent kinetic energy and divergence of velocity fluctuations indicate that turbulence levels get amplified in the vicinity of the blast wave due to local compression and get suppressed in the core due to expansion there. This trend is supported by linear analysis of turbulence going through a shock wave (Mahesh et al. 1995,1997).

- Statistics for vorticity fluctuations indicate amplification in vorticity levels near the leading edge of the plasma where the mean vorticity levels were observed to be high.

This report is organized as follows. Section 2 describes details of the algorithm used, validation tests performed and numerical issues addressed. Section 3 contains simulation results. Section 3.1 describes the spherical idealization of the plasma while section 3.2 contains description of the tear–drop shaped idealization of the plasma. Section 3.3 describes interaction of the spherical idealization of the plasma with background isotropic turbulence. Section 3.4 contains description of the tear–drop shaped idealization of the plasma interacting with isotropic turbulence in the background. A short summary is presented in section 4.

2 Simulation methodology

2.1 Algorithm description

The governing equations are the continuity, and compressible Navier–Stokes equations applied to a real gas,

$$\frac{\partial \rho}{\partial t} + \frac{\partial \rho u_i}{\partial x_i} = 0, \tag{1}$$

$$\frac{\partial \rho u_j}{\partial t} + \frac{\partial \rho u_j u_i}{\partial x_i} = -\frac{\partial}{\partial x_i}\left[p\delta_{ij} - \frac{\mu(T)}{Re}\left(\frac{\partial u_i}{\partial x_j} + \frac{\partial u_j}{\partial x_i} - \frac{2}{3}\frac{\partial u_k}{\partial x_k}\delta_{ij} \right) \right], \tag{2}$$

$$\frac{\partial \rho e_T}{\partial t} + \frac{\partial \rho e_T u_i}{\partial x_i} = \frac{\partial}{\partial x_i}\left[-pu_i + \frac{\mu(T)}{Re}\left(\frac{\partial u_i}{\partial x_j} + \frac{\partial u_j}{\partial x_i} - \frac{2}{3}\frac{\partial u_k}{\partial x_k}\delta_{ij} \right)u_j \right] + \tag{3}$$
$$\frac{\partial}{\partial x_i}\left(\frac{\kappa(T)}{(\gamma-1)RePr}\frac{\partial T}{\partial x_i} \right)$$

where all the variables are non–dimensionalized with respect to their initial background values.

$$x_i = x_i{}^* / L_0{}^*, \qquad u_i = u_i{}^* / c_0{}^*, \qquad t = t^* c_0{}^* / L_0{}^*, \tag{4}$$
$$\rho = \rho^* / \rho_0{}^*, \qquad p = p^* / \rho_0{}^* c_0{}^{*2}, \qquad T = T^* / T_0{}^*$$
$$\mu(T) = \mu(T)^* / \mu_0{}^*, \qquad \kappa(T) = \kappa(T)^* / \kappa_0{}^*.$$

Here, the subscript '0' denotes initial background values and the superscript, '*' denotes dimensional variables. L_0^* is the length scale and is obtained by comparing the non–dimensional length of the plasma region used in the simulations to the actual dimensional length of the plasma. c_0^* is the speed of sound based on initial background temperature; i.e.

$$c_0{}^* = (\gamma_0 R_0{}^* T_0{}^*)^{1/2}. \tag{5}$$

$\mu(T)^*$ and $\kappa(T)^*$ are dimensional coefficients of viscosity and thermal conductivity obtained by assuming an equilibrium model for air (figure 2).
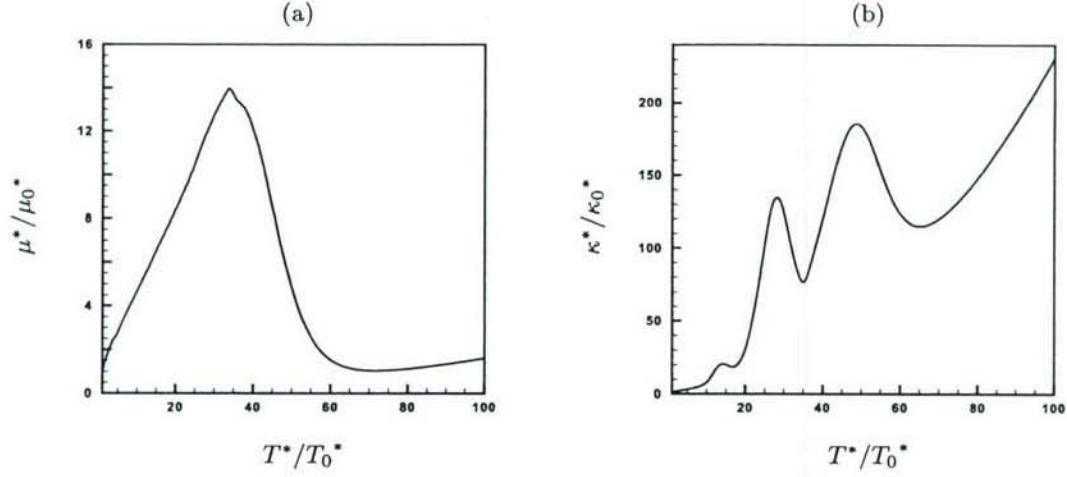The equation of state is

Figure 2: (a) Variation of the coefficient of viscosity μ with temperature T. (b) Variation of the coefficient of thermal conductivity κ with temperature T.

$$p = \rho R(T)T, \qquad (6)$$

where

$$R(T) = R^*(T)/\gamma_0 R_0, \qquad (7)$$

and the variation of R^* with temperature is shown in figure 3b. The total energy is related to internal energy and kinetic energy as

$$\rho e_T = \rho e + \frac{1}{2}\rho u_i u_i. \qquad (8)$$

and temperature is obtained form internal energy using the equilibrium dependence of internal energy on temperature shown in figure 3a.
The Reynolds number and Prandtl number are given by

$$Re = \rho_0^* c_0^* L_0^* / \mu_0^*, \quad Pr = \mu_0^* c_{p0}^* / \kappa_0^*. \qquad (9)$$

c_{p0}^* is the specific heat at constant pressure at $T^* = T_0^*$.
The Navier–Stokes equations are solved using Fourier methods to compute the spatial derivatives. Any variable f is discretely represented as

$$f(x_1, x_2, x_3) = \sum_{k_1=-N_1/2}^{N_1/2-1} \sum_{k_2=-N_2/2}^{N_2/2-1} \sum_{k_3=-N_3/2}^{N_3/2-1} \hat{f}(k_1, k_2, k_3) e^{(k_1 x_1 + k_2 x_2 + k_3 x_3)} \qquad (10)$$
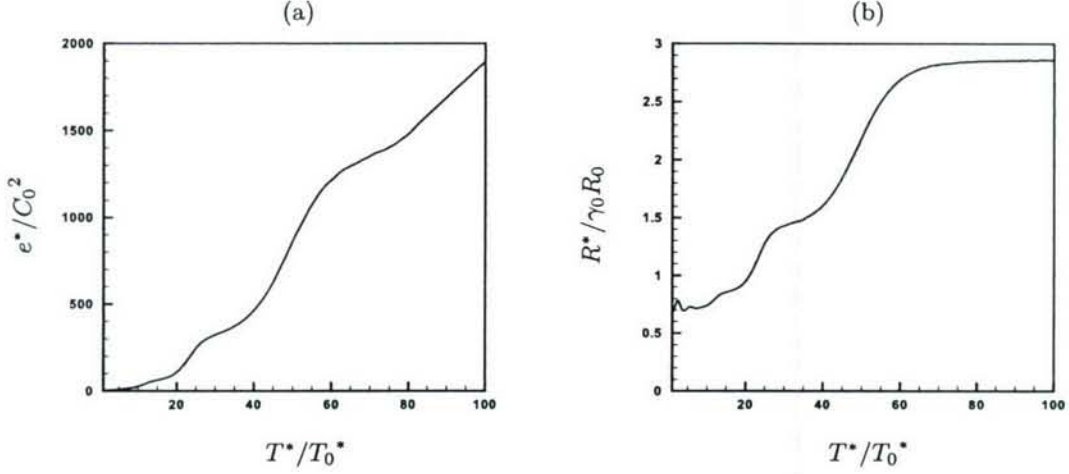
8

Figure 3: (a) Variation of internal energy e with temperature T, (b) Variation of R with temperature T.

where $\hat{f}(k_1, k_2, k_3)$ are the Fourier coefficients of f, and N_1, N_2 and N_3 are the number of points used to discretize the domain along x_1, x_2 and x_3 respectively. The Fourier coefficients of the spatial derivatives are therefore

$$\widehat{\frac{\partial f}{\partial x_\alpha}} = ik_\alpha \hat{f}, \quad \widehat{\frac{\partial^2 f}{\partial x_\alpha x_\alpha}} = -k_\alpha^2 \hat{f}. \tag{11}$$

A collocated approach is used, and the solution is advanced in time using a fourth order Runge–Kutta scheme. The skew–symmetric form of the convection terms

$$\frac{\partial fg}{\partial x_j} = \frac{1}{2}\left[\frac{\partial fg}{\partial x_j} + f\frac{\partial g}{\partial x_j} + g\frac{\partial f}{\partial x_j}\right], \tag{12}$$

is used to suppress aliasing errors resulting from the nonlinear convection terms (Blaisdell 1991). The above algorithm is implemented for parallel platforms using MPI. The library FFTW is used to compute Fourier transforms, and a pencil data structure is used. Each processor stores data along the entire extent of the x_1- direction, while data along the x_2- and x_3- directions are equally distributed among the processors. Fourier transforms along the x_1- direction are therefore readily computed, while transforms in the other directions require that the data be transposed prior to transforming.

2.2   Shock capturing

Recall that a strong shock wave propagates through the flow domain, when energy is added instantaneously. Experiments in laser induced breakdown (Yan

9

et al 2003) show that the maximum temperature in the core is very high. This leads to sharp gradients in the flow variables. Since the flow solver uses spectral methods for spatial discretization, resolving these sharp gradients requires a highly refined mesh. The computational cost therefore increases significantly with increasing core temperatures. The Fourier spectral method is therefore combined with a shock capturing scheme proposed by Yee et al (1999), to avoid resolution of the shock thickness.

The shock capturing scheme is based on the finite volume methodology, and is applied as a corrector step to the Fourier discretization used in this work. In the first step, the predicted form of the solution vector is obtained using Fourier methods as discussed in the previous section. This solution vector is then corrected using the filter numerical fluxes obtained by using a characteristic based filter

$$U^{n+1} = \widehat{U}^{n+1} + \Delta t \left[\frac{1}{\Delta x} \left(\widetilde{F}^{\star}_{i+1/2,j,k} - \widetilde{F}^{\star}_{i-1/2,j,k} \right) + \right. \tag{13}$$

$$\left. \frac{1}{\Delta y} \left(\widetilde{G}^{\star}_{i,j+1/2,k} - \widetilde{G}^{\star}_{i,j-1/2,k} \right) + \frac{1}{\Delta z} \left(\widetilde{H}^{\star}_{i,j,k+1/2} - \widetilde{H}^{\star}_{i,j,k-1/2} \right) \right]$$

The filter numerical flux vector is of the form

$$\widetilde{F}^{\star}_{i+1/2,j,k} = \frac{1}{2} R_{i+1/2,j,k} \phi^{\star}_{i+1/2,j,k} \tag{14}$$

where R is the right eigen vector matrix. The elements of $\phi^{\star}$ are denoted by $\phi^{l\star}$ and are given by

$$\phi^{l\star}_{i+1/2,j,k} = \kappa \theta^{l}_{i+1/2,j,k} \phi^{l}_{i+1/2,j,k} \tag{15}$$

The parameter κ is problem dependent and lies between 0.03 and 2 (Yee et al 1999). $\kappa = 1.0$ has been used in the simulations. The function $\theta^{l}_{i+1/2,j,k}$ is the Harten switch (Harten 1978) and depends on the Left eigen vector matrix L. The formulation used for $\phi^{l}_{i+1/2,j,k}$ is given by the Harten–Yee upwind TVD form (Yee et al 1999).

However for high temperature flows, separate treatment needs to be provided to the computation of the eigen vector matrices R and L. The specific heats at constant pressure and volume C_P and C_V are no longer constants but depend strongly on temperature (figure 4). Also the internal energy and enthalpy can no longer be obtained from the simple relations

$$e = C_V T \quad ; \quad h = C_P T \tag{16}$$

The sound speed is no longer obtained by
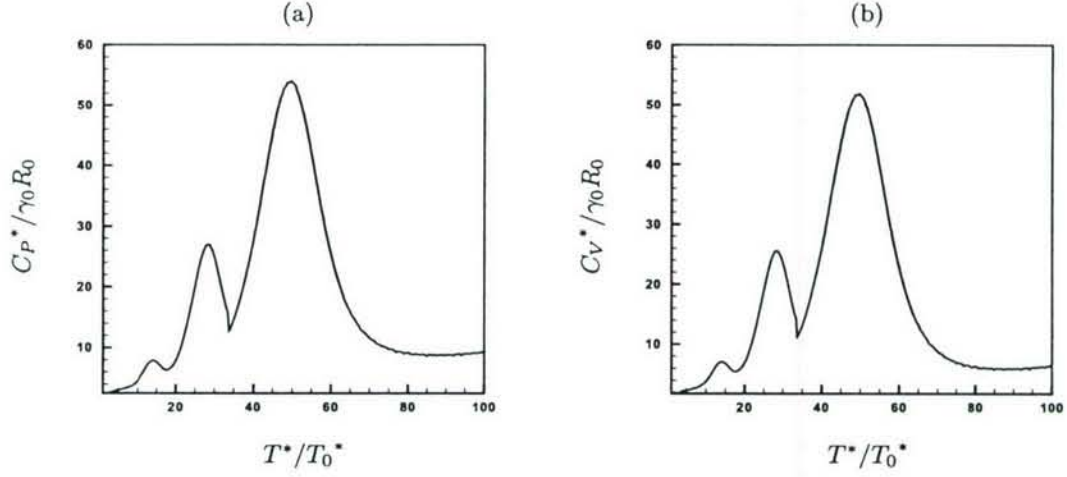
$$c = (\gamma R T)^{1/2} \tag{17}$$

10

Figure 4: (a) Variation of C_P with temperature T, (b) Variation of C_V with temperature T.

and R no longer remains a constant but becomes a function of temperature (figure 3b). Thus to compute the eigen vector matrices, the Jacobian matrix $\frac{\partial \mathbf{F}}{\partial \mathbf{U}}$ needs to be recomputed. Here $\mathbf{F}$ denotes the flux vector and $\mathbf{U}$ denotes the vector of the conserved variables.

Let the equation of state for the gas be given by

$$p = \rho R(T) T. \tag{18}$$

Then the elemental change in pressure dp can be written as

$$dp = RT d\rho + \rho \left(R + T \frac{dR}{dT} \right) dT \tag{19}$$

Now since $e = e(T)$ only

$$dT = \left(\frac{dT}{de} \right) de \tag{20}$$

Where the internal energy e can be written in terms of the conservative variables u_i. Using the above relations the Jacobian matrix along the x-direction can be computed as

$$\mathbf{J_X} = \begin{pmatrix} 0 & 1 & 0 & 0 & 0 \\ (-u^2 + RT - A(e - e_k)) & (2 - A) * u & -Av & -Aw & A \\ -vu & v & u & 0 & 0 \\ -wu & w & 0 & u & 0 \\ -(e_0 + A(e - e_k))u & (e_0 + RT - Au^2) & -Auv & -Auw & (1 + A)u \end{pmatrix}$$

Where

$$e_0 = e + e_k \tag{21}$$

11

is the total energy and e_k is the kinetic energy given by

$$e_k = \frac{1}{2} u_i u_i \tag{22}$$

And the factor A is given by

$$A = \left(R + T \frac{dR}{dT} \right) \frac{dT}{de} \tag{23}$$

Similar Jacobian matrices can be computed along y and z directions as well. Note that evaluation of these Jacobian matrices need knowledge of the variation of e and R with temperature. This can be obtained for air assuming it to be composed of several species present under conditions of chemical and thermal equilibrium (figure 3).

The eigen values of the above Jacobian matrix is given by

$$\lambda = (\quad u - c_1, \quad u \quad u + c_1, \quad u \quad u \quad)$$

Where the modified speed of sound c_1 is given by

$$c_1 = ((1 + A)RT)^{1/2} \tag{24}$$

it may be noted that c_1 reduces back to c for the low temperature conditions and the Jacobian matrix reduces back to the low temperature Jacobian. The modified sound speed depends on the variation of e and R with T through the factor A. c_1 has been computed and compared to data for speed of sound obtained assuming air as a mixture of multiple species in equilibrium (figure 5). A reasonable comparison is obtained up to $T^* = 15000K$.

The right eigen vector matrix $\mathbf{R}$ can be obtained by solving the system of equations

$$[J]R_i = \lambda_i R_i \tag{25}$$

Where λ_i are the individual eigen values and R_i are the eigen vectors. Define a set of variables e_1 and e_2 such that

$$e_1 = \frac{c_1{}^2}{A(A+1)} \tag{26}$$

And

$$e_2 = e - e_1 \tag{27}$$

Also define $e_k{}^*$ such that

$$e_k{}^* = e_k - e_2 \tag{28}$$

Then the right eigen vector matrix for the x direction is obtained as

12

$$
\mathbf{R_X} = \begin{pmatrix}
1 & 1 & 1 & 0 & 0 \\
u - c_1 & u & u + c_1 & 0 & 0 \\
v & v & v & -1 & 0 \\
w & w & w & 0 & 1 \\
(h_0 - c_1 u) & e_k{}^\bullet & (h_0 + c_1 u) & -v & w
\end{pmatrix}
$$

Where h_0 is the total enthalpy given by

$$
h_0 = h + e_k. \tag{29}
$$

Then the left eigen vector matrix is obtained as

$$
[L] = [R]^{-1} \tag{30}
$$

and for the x-direction it is given by

$$
\mathbf{L_X} = \begin{pmatrix}
\frac{A e_k{}^\bullet + c_1 u}{2 c_1{}^2} & -\frac{A u + c_1}{2 c_1{}^2} & -\frac{A v}{2 c_1{}^2} & -\frac{A w}{2 c_1{}^2} & \frac{A}{2 c_1{}^2} \\
\frac{c_1{}^2 - A e_k{}^\bullet}{c_1{}^2} & \frac{A u}{c_1{}^2} & \frac{A v}{c_1{}^2} & \frac{A w}{c_1{}^2} & -\frac{A}{c_1{}^2} \\
\frac{A e_k{}^\bullet - c_1 u}{2 c_1{}^2} & -\frac{A u - c_1}{2 c_1{}^2} & -\frac{A v}{2 c_1{}^2} & -\frac{A w}{2 c_1{}^2} & \frac{A}{2 c_1{}^2} \\
v & 0 & -1 & 0 & 0 \\
-w & 0 & 0 & 1 & 0
\end{pmatrix}
$$

Similarly eigen vectors R_Y, R_Z, L_Y and L_Z can be computed along the y and z directions respectively. A more generalized derivation that applies to generalized geometries is presented in the Appendix.

2.3   Logarithm formulation of the continuity equation

When laser energy is added to a flow at rest, there is noticeable expansion at the core. This results in very small values of density at the core. When the continuity equation was advanced in time with density as the dependent variable, the solution was found to become unstable. It was therefore decided to solve for the logarithm of density as the variable. Define

$$
v = \log \rho \qquad \Rightarrow \qquad \rho = e^v \tag{31}
$$

The continuity equation becomes

$$
\frac{\partial v}{\partial t} + u_i \frac{\partial v}{\partial x_i} = -\frac{\partial u_i}{\partial x_i}, \tag{32}
$$

Note that ρ is always positive when computed as e^v, even for very small values of ρ. The $\log \rho$ formulation of the continuity equation therefore makes the solution stable in regions of very low density.
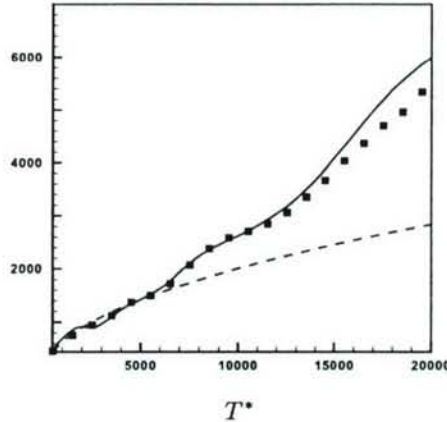
Figure 5: (a) Comparison of c_1 with data for speed of sound, ———— : speed of sound obtained from data, ▪ : computed speed of sound c_1, ---- : $c = (\gamma_0 R_0 T)^{1/2}$

2.4 Validation Results

The solver with shock capturing and the $\log \rho$ formulation for the continuity equation is validated using a periodic shock tube problem and isotropic turbulence. Figure 6a shows instantaneous profiles of the solution for the periodic shock tube problem. A region of high density fluid is located at the center of a tube. This region is separated from low density regions of the same fluid on either side. The initial density jump is from 0.3 to 3 and viscosity in the problem is 0.005. The initial pressure profile is obtained from the ideal gas law, keeping temperature constant. This initial condition generates shock waves, which propagate in either direction. Density, pressure and temperature profiles obtained at $t = 1.0$ using shock capturing and the $\log \rho$ formulation are compared to those obtained without using these formulations. The profiles show good agreement. Figure 6b shows decay of turbulent kinetic energy for isotropic turbulence. The initial velocity fluctuations are generated using Rogallo's (1981) method. The initial energy spectrum is top-hat, with energy in wave numbers between 8 and 16. The turbulent Reynolds number is 50 and the fluctuation Mach number is 0.3. Note that decay of turbulent kinetic energy in time with, and without the $\log \rho$ formulation of the continuity equation compare well.

2.5 Validity of Navier–Stokes simulation

This work considers only the thermal effects of the plasma, assuming that these effects are decoupled from the effects of charged particles in the flow. This can be justified by recalling that the time–scale for plasma generation is significantly
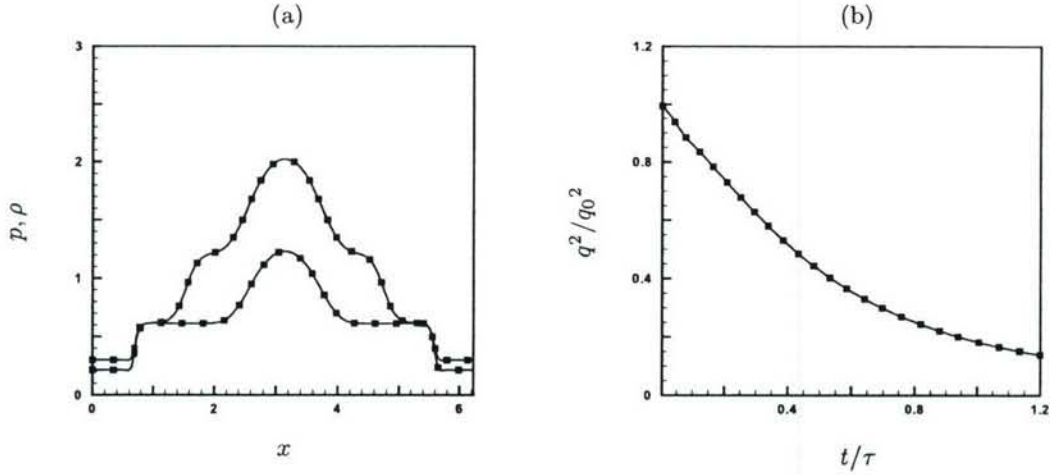
14

Figure 6: (a) Comparison of profiles for the periodic shock tube problem at $t = 1.0$, ——— without shock capturing and $\log \rho$ formulation, ■ with shock capturing and $\log \rho$ formulation, (b) Decay of turbulent kinetic energy for isotropic turbulence. Time is non–dimensionalized by the eddy turn over time τ, ——— without $\log \rho$ formulation, ■ with $\log \rho$ formulation.

smaller than the time–scale on which the gas–dynamic effects on the flow are observed. Also at the end of plasma formation, the electron number density decreases sharply due to electron recombination. Typically for ND–YAG laser plasma at an ambient pressure of 1 atmosphere, the electron number density decreases to less than one tenth of it's maximum value in 100 nanoseconds. So at the end of plasma formation, all that is left is a region of high temperature and pressure. If the simulations are initialized with the profiles of thermodynamic quantities at the end of the plasma formation process, then the effects of charged particles will not be very significant.

Note that the temperature in the core of the plasma is quite high at initial times. This leads to finite rate chemical reactions in the core of the plasma. Heat absorbed or released during these reactions affects the thermodynamic properties in the core. However, the core cools down fast. Also, temperatures near the blast wave are much lower compared to those in the core of the plasma. Thus for the purpose of studying the properties of the blast wave, the effects of chemistry would not be significant. This will be demonstrated by comparing shock radius and jumps in the thermodynamic quantities to experimental results. Also, the ideal gas law has been assumed, and fluid properties like viscosity and thermal conductivity have been assumed to vary as a power law with temperature. Again, these assumptions hold after an initial time when the plasma generation is complete. Local thermodynamic equilibrium conditions have been assumed. These conditions are reasonably valid after a few nanoseconds owing to the high temperatures involved.
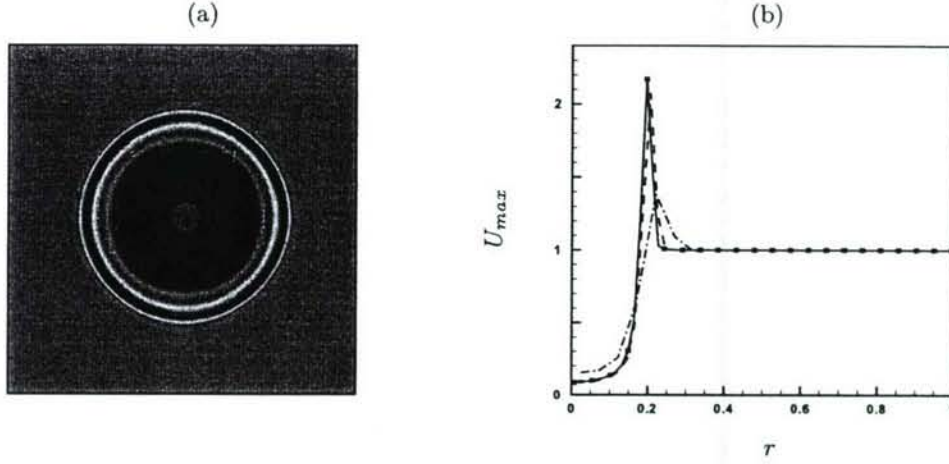
15

Figure 7: (a) Contours of pressure showing propagation of blast wave in flow at rest, (b) Illustration of grid convergence. Radial profiles of density for different mesh spacing, ———— : $\Delta x = 0.0157$, ▪ : $\Delta x = 0.0196$, ---- : $\Delta x = 0.0245$, —·— : $\Delta x = 0.0491$.

3 Results

3.1 Spherical idealization

A spherical region of the flow is heated at the center of the domain. The initial temperature distribution has a Gaussian profile:

$$\underbrace{T - 1}_{\Delta T} = \underbrace{(T_0 - 1)}_{\Delta T_0} e^{-r^2/r_0^2} \tag{33}$$

where the temperatures are non-dimensionalized by the ambient temperature. ΔT is the local temperature excess over the ambient value, and ΔT_0 is the maximum temperature excess at the core of the plasma. r is the radial distance from the center and r_0 is the cut–off radius for the Gaussian profile, chosen to be $\pi/20$ in a domain of 2π.

Energy is deposited at the center of the flow domain by increasing the temperature and pressure locally at constant density. The initial energy deposited ΔE can be related to ΔT_0 by integrating,

$$E = \int_0^\infty \rho_\infty c_v \Delta T 4\pi r^2 dr, \tag{34}$$

which yields

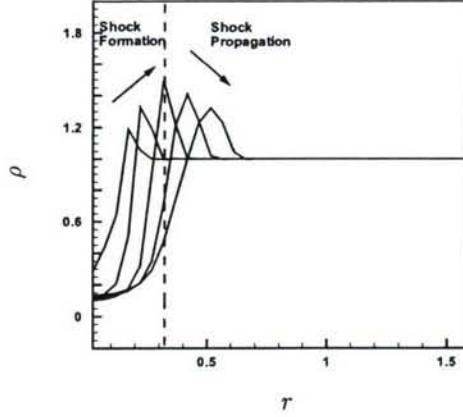$$E = \Delta T_0 \pi^{3/2} \rho_\infty c_v r_0^3. \tag{35}$$

16

Figure 8: Radial profiles of density at $t = 0.014$, 0.034, 0.079, 0.141 and 0.218 for $\Delta T_0 = 90$ showing shock formation and propagation.

Simulation results are obtained for ΔT_0 ranging from 30 to 300. Figure 7a shows contours of pressure at $t = 1.2$ for a maximum temperature excess of 300 in the core. A spherically symmetric shock front is seen to propagate, compressing the flow ahead of it, while the flow behind it expands. Since the problem is spherically symmetric, mean values of the flow variables are computed in a radially symmetric manner, and plotted as a function of radial distance from the center of the plasma.

The jump in flow variables across the shock wave will be incorrectly predicted if the mesh used in the simulations is not fine enough to resolve the sharp gradients at the shock front. A grid convergence study was performed. Figure 7b shows the radial profile of density at the instant of time when it acquires its maximum value. The initial temperature ratio in the core, $\Delta T_0 = 300$. The first simulation used a coarse mesh ($\Delta x = 0.0491$). The mesh size was then refined successively until the solution did not change significantly for two successive mesh refinements. The density profiles obtained for different values of the mesh spacing are shown in figure 7b. The solution is observed to be grid converged for $\Delta x = 0.0196$. This mesh was used for all simulations reported in this section.

3.1.1   Shock formation and shock propagation

The post–energy deposition process can be divided into two parts - shock formation and shock propagation. Figure 8 shows radial profiles of density at different instants of time. Time is non–dimensionalized with respect to a reference time scale t_r which is obtained from the ratio of a reference length scale l_r and reference velocity scale c_r. For the spherical idealization l_r is $20/\pi$ times the initial radius of the plasma region, while c_r is the background speed of sound. There is
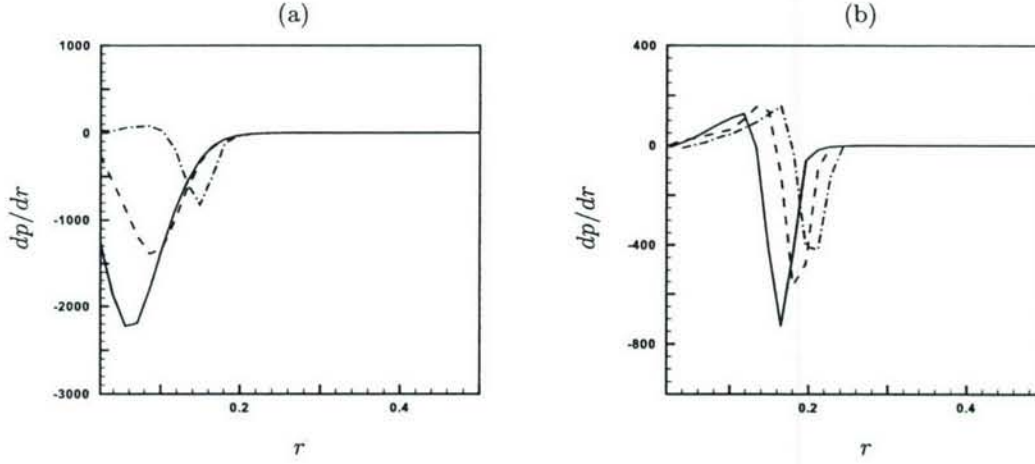
17

Figure 9: (a) Radial profiles of pressure gradients during the shock formation process. ———— : $t = 0.001$, - - - - : $t = 0.005$, — - — : $t = 0.013$, (b) Radial profiles of pressure gradients during the shock propagation process. ———— : $t = 0.017$, - - - - : $t = 0.023$, — - — : $t = 0.029$.

an initial period of time during which the intensity of the shock front increases with time, indicating formation of the shock. Once shock formation is complete, the shock wave propagates radially into the background gas, its strength decreasing as a result.

Shock formation and propagation can be explained by the large pressure gradients generated by energy deposition. Energy is deposited in the form of internal energy of the fluid elements by increasing the temperature at constant density. Since the initial temperature profile is a Gaussian, the resulting pressure profile is also a Gaussian. The gradients in pressure thus formed, accelerate the flow radially, through the conservation of momentum. Thus the internal energy of the fluid elements is converted into kinetic energy through the pressure gradients in the flow. This results in formation of a shock wave whose strength initially increases. The pressure gradients then drive the shock wave radially into the background gas, and the strength of the shock decreases.

Figure 9a shows radial profiles of pressure gradients at different instants during shock formation. Note that the gradients in pressure are initially negative, indicating that the pressure is highest at the center of the plasma. At later instants, the pressure gradients acquire positive and negative values, indicating that a shock front has begun to form, and the peak value of pressure is no longer at the center of the domain. Figure 9b shows radial profiles of the pressure gradients as the shock propagates. Pressure gradients at three subsequent instants of time are shown. Note that both the positive and negative values of pressure gradients decrease in time due to the radial spreading of the shock wave.

Figure 10a shows the variation of shock Mach number in time for $\Delta T_0 = 300$,
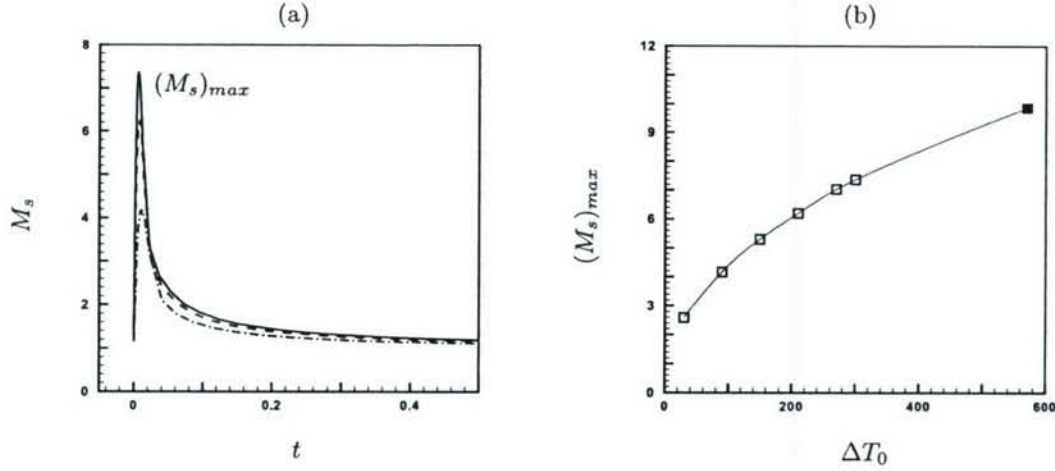
18

Figure 10: (a) Variation of shock Mach number with time ———: $\Delta T_0 = 300$, ————: $\Delta T_0 = 210$, —·—: $\Delta T_0 = 90$, (b) Variation of maximum shock Mach number with ΔT_0, □: simulation results, ■: Experimental data (Yan et al 2003).

210 and 90. The initial steep increase in the shock Mach number depicts shock formation. The later gradual decrease in shock Mach number depicts the radial propagation of the shock. The shock Mach number attains a maximum value at the end of shock formation. The values of shock Mach number increase with increase in energy deposited.

Figure 10b shows the maximum shock Mach number for different values of ΔT_0. The shock Mach number can be computed using the relation

$$U_s = \frac{\gamma + 1}{4}U + ((\frac{\gamma + 1}{4}U)^2 + c_\infty^2)^{1/2}, \qquad (36)$$

for the shock velocity U_s. Here, U is the velocity behind the shock front and c_∞ is the speed of sound ahead of it. The maximum shock Mach number is plotted for ΔT_0 ranging from 30 to 300. As expected, M_s increases with energy deposited in the flow. A power law fit is obtained and extrapolated to higher temperatures. The prediction of maximum shock Mach number for higher temperatures matches well with data from experiments at $\Delta T_0 = 570$ (Yan et al 2003).

Figure 11a shows shock formation time as a function of ΔT_0. Figure 11b shows shock propagation time for different values of ΔT_0. Here, shock propagation time is the time required for the shock front to reach a point where $r/r_0 = 40/\pi$, r_0 being the initial size of the plasma. Both shock formation and shock propagation time decrease with increase in ΔT_0. Comparison of figures 11a and 11b shows that for a given ΔT_0 the shock propagation time is 2 to 3 orders of magnitude larger than the corresponding shock formation time. This can also
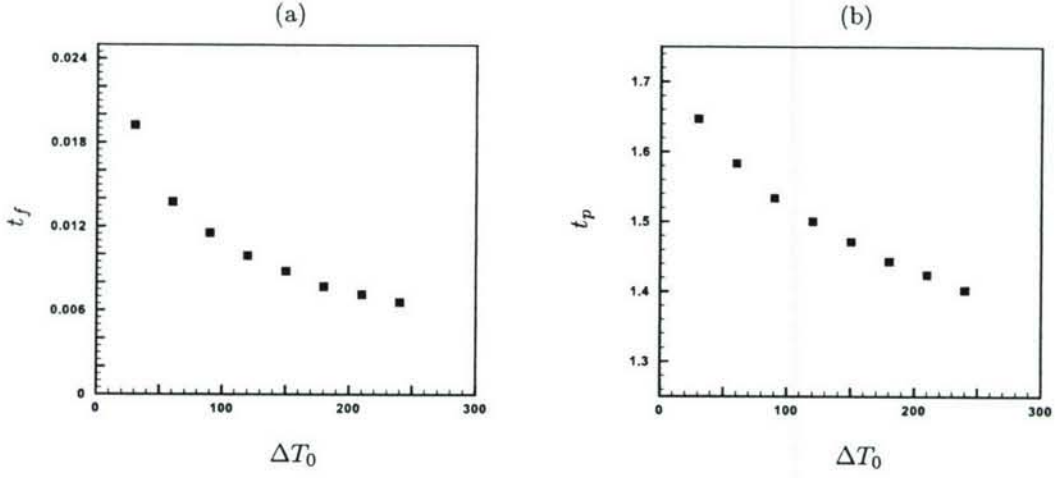
19

Figure 11: (a) Shock formation and (b) Shock propagation time for different ΔT_0.

be observed in figure 10. In fact, for $\Delta T_0 = 300$, the shock formation time becomes comparable to the time scale in which the plasma generation occurs and so the Navier–Stokes model may not accurately represent some of the flow features.

3.1.2 Comparison to strong shock solution

Based on dimensional arguments, Taylor (1950) and Sedov (1959) independently proposed a similarity solution for the point blast problem. The process was idealized as a sudden release of energy E at a point. Further, it was assumed that the resulting shock wave is so strong that the pressure and sound speed of the background medium are negligible compared to the pressure and velocity of the shock wave. Based on these assumptions, the only dimensional parameters involved in this problem are the amount of energy deposited E, and the density of the background medium ρ_∞. The strong shock jump conditions (Taylor 1950, Sedov 1959) apply; i.e.

$$u = \frac{2}{\gamma+1}U_s \quad , \quad \rho = \frac{\gamma+1}{\gamma-1}\rho_\infty \quad , \quad p = \frac{2}{\gamma+1}\rho_\infty U_s^{\,2} \tag{37}$$

where u, ρ and p are the velocity, density and pressure immediately behind the shock wave, and U_s is the shock velocity. Then based on dimensional arguments, the shock radius R_s at any time t is given by

$$R_s(t) = k\left(\frac{E}{\rho_\infty}\right)^{1/5} t^{2/5} \tag{38}$$
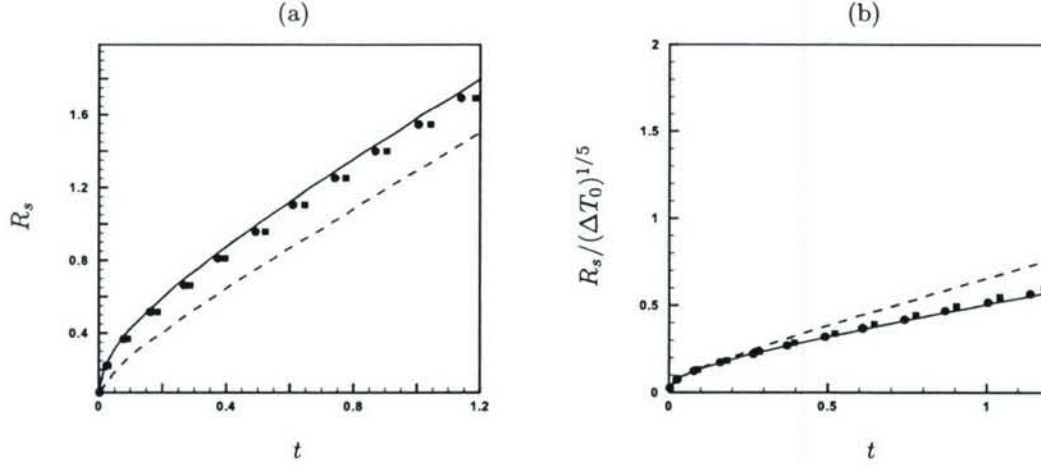
20

Figure 12: (a) Variation of shock radius with time, (b) Variation of $R_s/(\Delta T_0)^{1/5}$ with time, ——— : $\Delta T_0 = 300$, • : $\Delta T_0 = 240$, ▪ : $\Delta T_0 = 180$, - - - - : $\Delta T_0 = 30$.

where k is a dimensionless number. The pressure and velocity immediately behind the shock front can be obtained from the jump conditions

$$p \;=\; \frac{8}{25}\frac{k^2\rho_\infty}{\gamma+1}\left(\frac{E}{\rho_\infty}\right)^{2/5}t^{-6/5}, \tag{39}$$

$$u \;=\; \frac{4}{5}\frac{k}{\gamma+1}\left(\frac{E}{\rho_\infty}\right)^{1/5}t^{-3/5}. \tag{40}$$

Simulation results for variation of shock radii in time for $\Delta T_0 = 300$, 240, 180 and 30 are shown in figure 12a. Note that from equation 35,

$$E \;\sim\; \Delta T_0. \tag{41}$$

Equations 41 and 38 suggest that if the strong shock solution were to apply, then all the curves in figure 12a should collapse into one single curve when $R_s/\Delta T_0^{1/5}$ is plotted against time. Figure 12b shows the variation of $R_s/\Delta T_0^{1/5}$ with time for $\Delta T_0 = 300$, 240, 180 and 30. It is clear that for an initial time all these curves collapse over one another, but with increasing time they start to separate. The lowest temperature ratio is the first to deviate. The curves would be expected to collapse only as long as the strong shock conditions are applicable. Smaller the energy deposited, sooner the shock strength weakens, and sooner the curve deviates from the strong shock limit.

Note that deviation from the strong shock limit leads to larger values of $R_s/\Delta T_0^{1/5}$ than would be expected from the strong shock solution. This can be explained
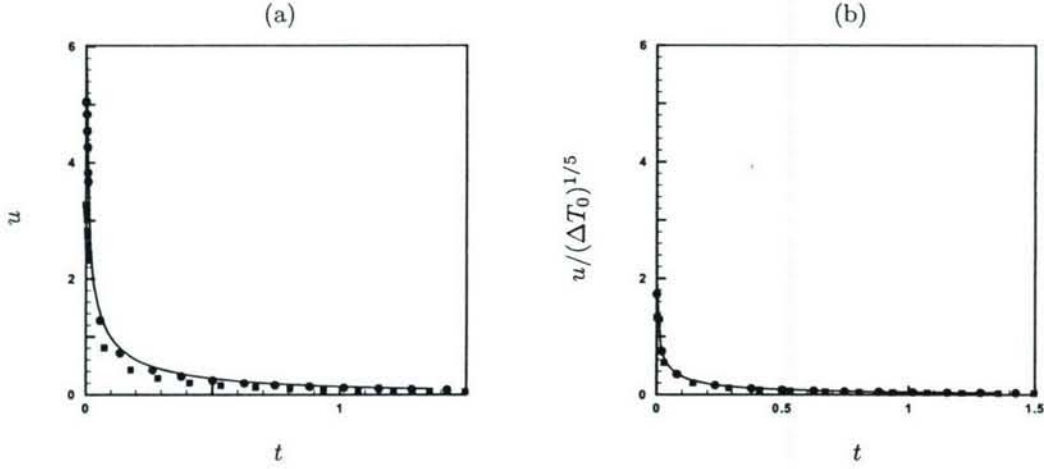
21

Figure 13: (a) Variation of velocity at the shock front against time, (b) Variation of $u/(\Delta T_0)^{1/5}$ against time, ——: $\Delta T_0 = 300$, •: $\Delta T_0 = 210$, ▪: $\Delta T_0 = 90$.

as follows. As the shock propagates radially, its strength decreases, and eventually it becomes an acoustic wave traveling at the speed of sound. Hence the other relevant limit for the time variation of shock radius is the acoustic limit which the shock wave eventually attains, regardless of the energy deposited in the flow. The time required to reach this limit, would however increase as the energy deposited increases. For the acoustic limit,

$$\frac{\partial R_s}{\partial t} = c_\infty \tag{42}$$

where c_∞ is the background speed of sound. Thus for the curves in figure 12b, the slope in the acoustic limit would be $c_\infty/\Delta T_0^{1/5}$. So, for smaller energy deposited in the flow the slope of the curve is larger in the acoustic limit, and hence the deviation from the strong shock limit is towards larger values of $R_s/\Delta T_0^{1/5}$.

Again, combining equations 41 and 40, it may be reasoned that in the strong shock limit, the curves of $u/\Delta T_0^{1/5}$ against time must collapse over one another for different values of ΔT_0. Figure 13a shows velocity immediately behind the shock front against time for $\Delta T_0 = 300$, 210 and 90. Figure 13b shows $u/\Delta T_0^{1/5}$ against time for $\Delta T_0 = 300$, 210 and 90. Collapse with the strong shock scaling is reasonable at initial times when the strong shock conditions are valid. However, at later instants of time, these curves deviate from the strong shock solution. This behavior can again be explained in terms of deviation from the strong shock limit towards the acoustic limit.
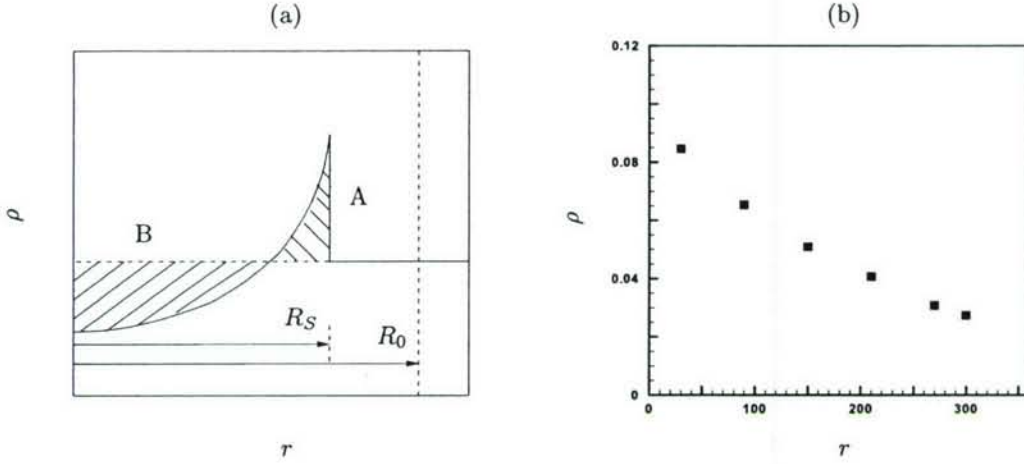
22

Figure 14: (a) Schematic to illustrate the conservation of mass within a control volume surrounding the shock wave, (b) Minimum density in the core for different amounts of energy deposited in the flow.

3.1.3 Behavior of the core

The strong shock solution solution predicts the density at the core to be zero. This would mean that the core has expanded to the extent that there is no mass left in the core. However for weaker conditions, as the density at the shock front keeps increasing during shock formation, the density in the core keeps decreasing. Once the shock formation is complete, the shock propagates down the domain with decreasing intensity. Hence density at the shock front starts decreasing and the density at the core simultaneously starts increasing (Figure 8).

This behavior can be explained by conservation of mass behind the shock front. Figure 14a shows a schematic for density variation behind the shock front. Consider a spherical control volume of radius R_0 around the shock-wave whose radius $R_S < R_0$. The integral form of the continuity equation is given by

$$\int_V \left[\frac{\partial \rho}{\partial t} + \frac{\partial \rho u_j}{\partial x_j} \right] dV = 0 \tag{43}$$

where V is the control volume under consideration. Since there is no mass flux in or out of the control volume, the second term in equation 43 becomes zero. Also assuming that the control volume is large, the shock front is confined within this volume for all time and so the control volume does not change with time. Then the time derivative in the first term of equation 43 can be taken outside the volume integral to obtain
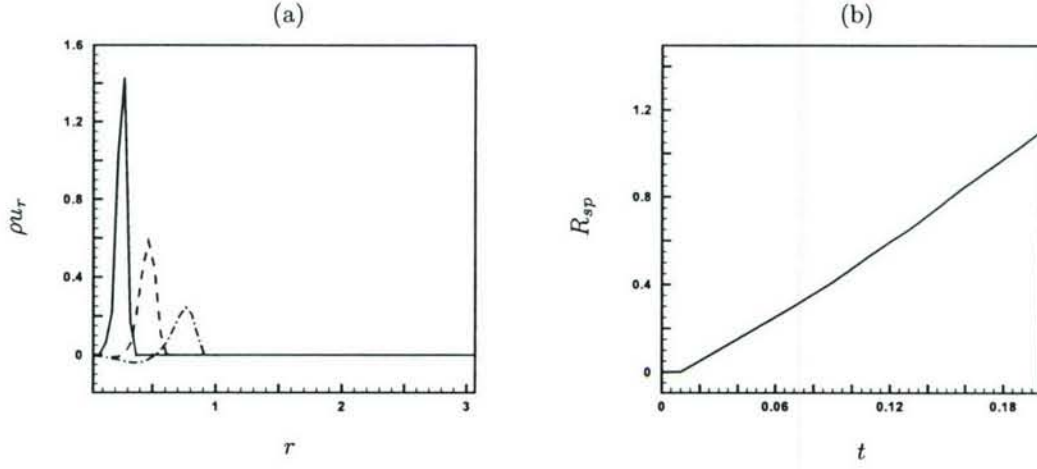
$$\int_V \rho \, dV = m_0 \tag{44}$$

23

Figure 15: (a) Radial profiles of ρu_r at different instants of time showing radial collapse of the flow field, ——— : $t = 0.051$, - - - - : $t = 0.186$, —·— : $t = 0.422$, (b) Radial location of the spherical stagnation front in time.
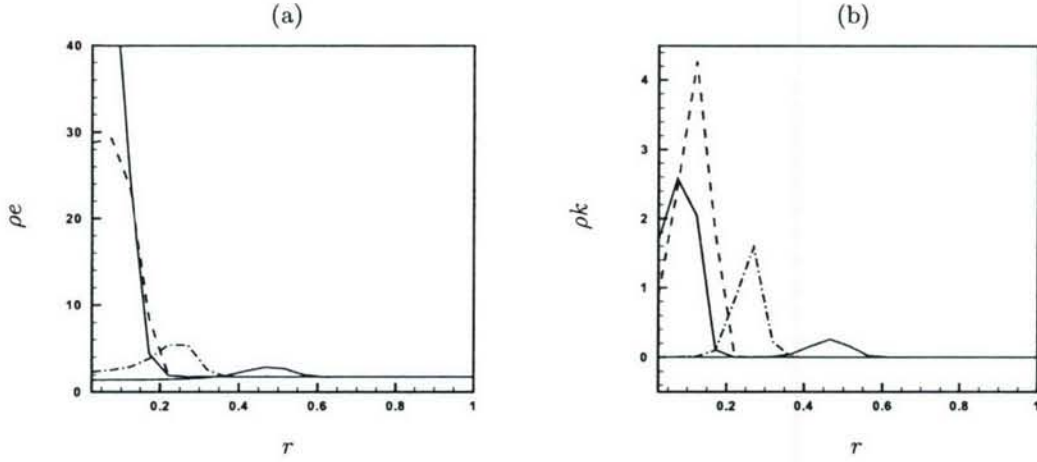

Figure 16: (a) Radial profiles of internal energy per unit volume at different instants of time, (b) Radial profiles of kinetic energy per unit volume at different instants of time, ——— : $t = 0.005$, - - - - : $t = 0.011$, —·— : $t = 0.051$, ········ : $t = 0.186$.
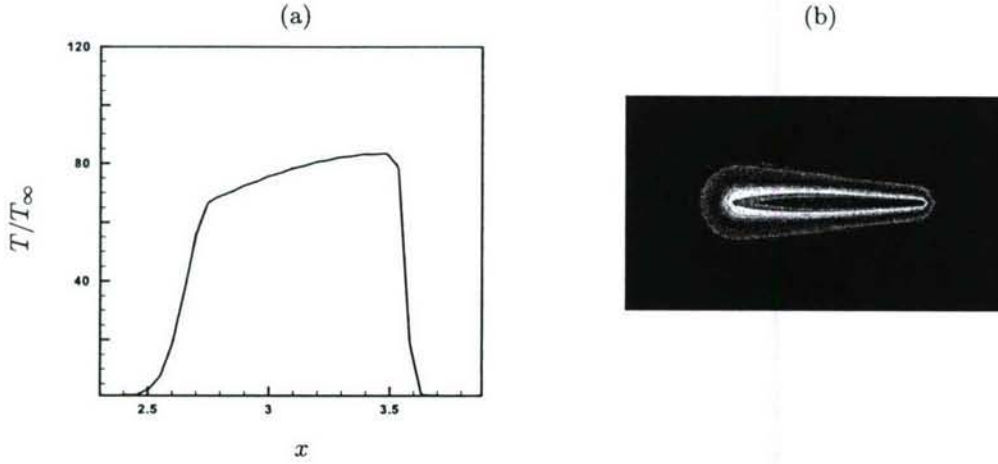
24

Figure 17: (a) Axial variation of the initial temperature profile, (b) Contour plot of initial temperature in a plane through the plasma axis.

where m_0 is a constant and is equal to the initial mass within the control volume. Thus total mass within the control volume is conserved at all times.

At the shock front, mass accumulates due to compression. This mass comes from the core, and hence the core experiences an expansion leading to decrease in density. During shock formation, mass accumulation at the shock front increases and so density in the core decreases. The reverse occurs during shock propagation. At any instant of time the accumulated mass at the shock front indicated by the shaded area A has to balance the deficit of mass in the core indicated by the shaded area B.

Figure 14b shows the minimum value of density at the core as a function of energy deposited. The minimum value of density is observed to decrease with increase in energy deposited in the flow. The trend suggests that in the strong shock limit, the density in the core will tend to be zero. However with large decrease in density, note that the continuum model used for the Navier–Stokes equations becomes less valid.

Note that as the shock front propagates out radially, the flow behind the shock front experiences a radial collapse. Figure 15a shows radial profiles of the convection flux, ρu_r, at different instants. The initial temperature ratio in the core, $\Delta T_0 = 90$. During formation of the shock wave, the flow expands outwards and no reverse flow is observed. However as the shock wave propagates into the background medium, the outward radial motion near the shock front is followed by a reverse radial flow in the core. Hence a spherical stagnation front is formed that separates the flow moving radially inwards from that moving radially outwards. The location of the stagnation front depends on the location of the shock front and moves outward in time. Figure 15b shows radial location of the spherical stagnation front, R_{sp}, as a function of time. The initial flat portion of the curve
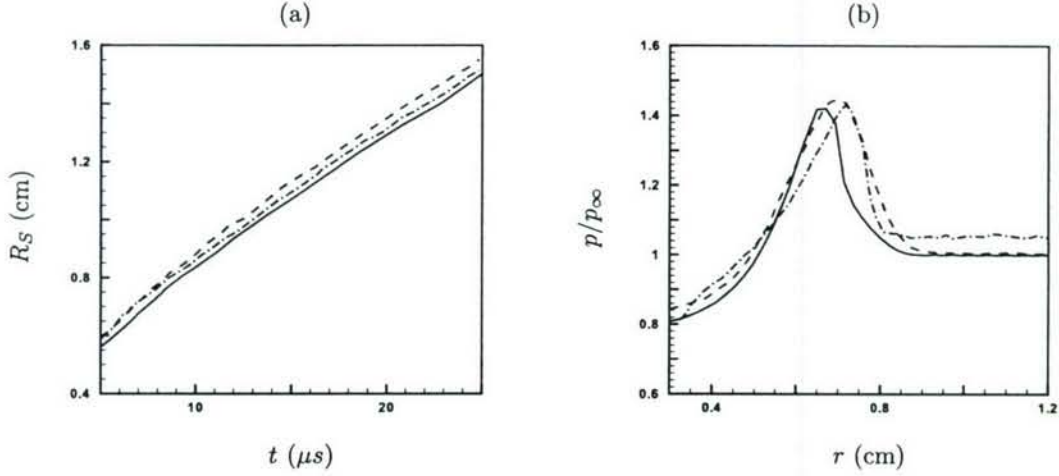
25

Figure 18: (a) Comparison of shock radius normal to the axis of the plasma, (b) Density profiles normal to the axis of the plasma at 10 μs ——— : simulation results, —·—· : experiment (Adelgren et al 2001), ———— : simulations of Kandala and Candler (2003).

represents formation of the shock wave when the flow expands radially outward only. As the reverse flow sets in the radial location of the stagnation front is observed to vary almost linearly with time.

Figure 16a shows radial profiles of internal energy per unit volume, ρe, at different instants of time. Radial profiles of kinetic energy per unit volume, ρk, are shown in figure 16b. The initial temperature ratio in the core, $\Delta T_0 = 90$. During formation of the shock wave, denoted by the first two profiles in figure 16, internal energy of the fluid elements is observed to get converted into kinetic energy leading to high velocities at the shock front. However as the shock propagates radially, the velocities at the shock front decrease and the kinetic energy is converted back to internal energy as observed in the last two profiles in figure 16. Note that within the control volume shown in figure 14a, the total energy is always conserved.

3.2 Tear–drop shaped idealization

This section contains results from simulations for the tear–drop shaped idealization of the plasma. Experiments in laser induced breakdown (Adelgren et al 2001, Yan et al 2003) show that the plasma is initially tear–drop shaped. Figure 17a shows the axial temperature distribution that is used to model the initial temperature profile for the tear–drop idealization of the plasma. Laser energy deposition is assumed to be symmetric about the laser axis. The temperature profile normal to the plasma axis is assumed to be a Gaussian. Figure 17b shows contours of temperature in a plane passing through the axis of the plasma. The
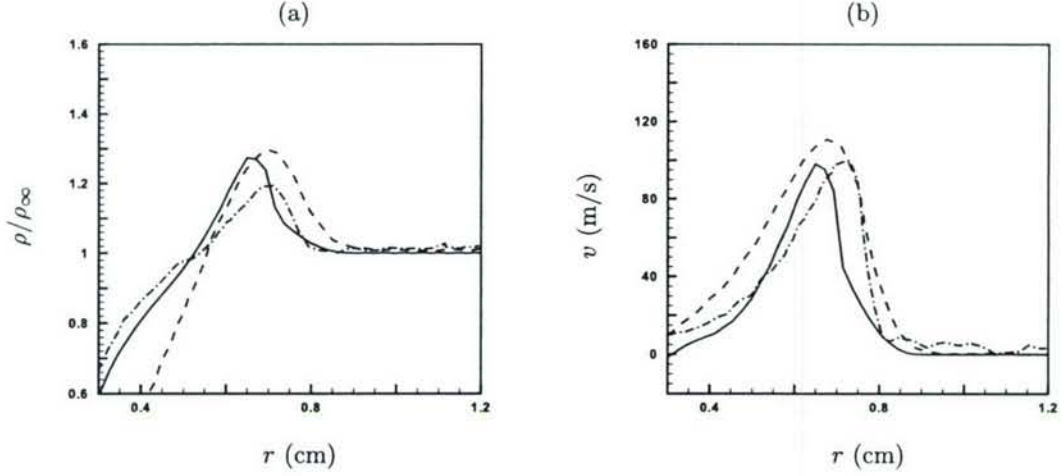
26

Figure 19: (a) Pressure profiles normal to the axis of the plasma at 10 μs, (b)velocity profiles normal to the axis of the plasma at 10 μs ——— : simulation results, ——·— : experiment (Adelgren et al 2001), ——-- : simulations of Kandala and Candler (2003).

initial temperature profile is similar to that observed in simulations of Kandala and Candler (2003).

3.2.1 Comparison to existing results

Figure 18a compares the shock radius normal to the plasma axis with experiment (Adelgren et al 2001) and simulation (Kandala and Candler 2003). Shock radius is defined by the outer edge of the pressure blast wave. Here the reference length scale l_r is obtained from the initial length of the plasma region to be 4.4075 mm and the reference velocity scale, c_r, is given by the background speed of sound. The reference time scale, t_r, is thus obtained to be 12.695 μs. The shock radius is seen to be slightly under–predicted. Figures 18b, 19a and 19b show pressure, density and velocity profiles normal to the axis of the plasma. The profiles are observed to peak slightly behind the peaks obtained in experiments. However, the peak values of density, pressure and velocity are well predicted. Also the behavior of density in the core is captured well. The reason for the differences may be attributed to the lack of accurate information about the variation of the initial temperature profile normal to the axis of the plasma due to which the temperature has been assumed to vary as a Gaussian in this direction. The reasonable agreement with existing data suggests that for the purpose of studying the properties of the blast wave and its effect on the surrounding fluid, the Navier–Stokes idealization might be adequate.
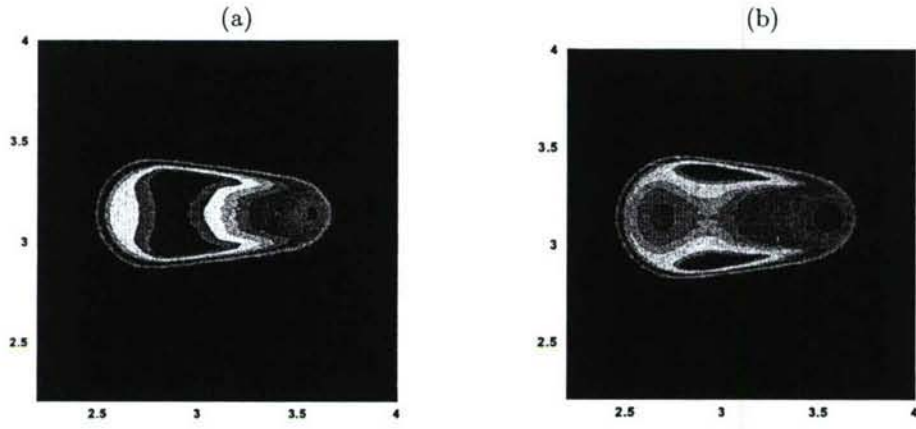
27

Figure 20: Pressure contours at $t = 0.02$ and 0.03 show formation of a distinct shock wave normal to the axis of the plasma.
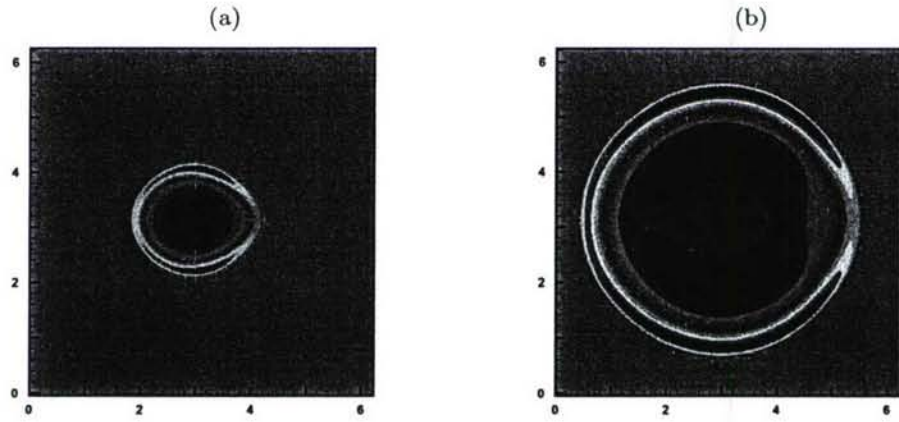

Figure 21: Pressure contours at $t = 0.36$ and 1.5 show that the blast wave is initially tear–drop shaped but become spherical in time.
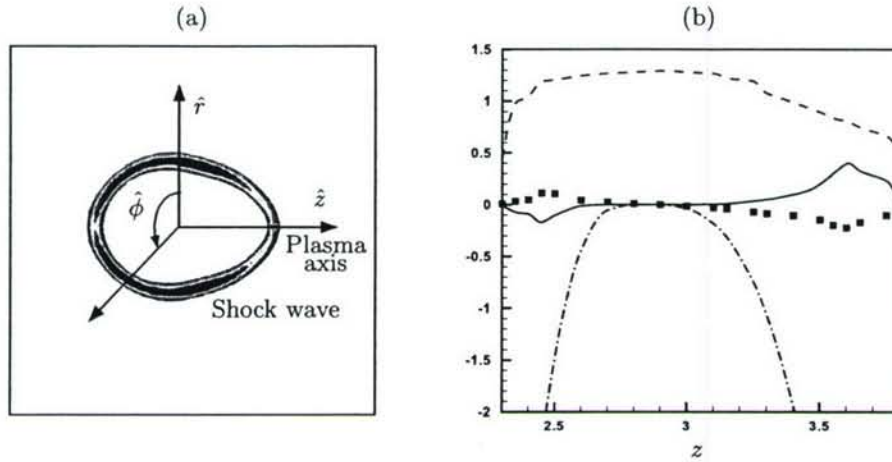
28

Figure 22: (a) Schematic showing propagation of a tear–drop shaped blast wave, (b) Generation of vorticity near leading and trailing edges of the plasma, ———— : vorticity jump across the shock wave, - - - - : shock strength, —·— : curvature of the shock front, ▪ : tangential velocity measured ahead of the shock.

3.2.2 Shock formation and propagation

As done for the spherical idealization, laser energy is added into the flow by increasing the temperature at constant density. Thus sharp gradients in pressure are generated in the flow. Again the entire process can be divided into the formation and propagation of a shock wave. Formation of the shock wave is shown in figure 20. Contours of pressure are shown at two successive instants of time. Due to the tear–drop shape of the plasma, pressure gradients normal to the plasma axis are larger compared to the gradients along the plasma axis. Thus fluid elements in a region normal to the axis begin to gain kinetic energy and a shock wave begins to form, and gradually steepen in intensity. The shock wave then propagates into the background gas with decreasing intensity. Figure 21 shows contours of pressure at two different instants of time during propagation of the shock wave. The blast wave is initially tear–drop shaped as observed in figure 21a. The stronger pressure gradients normal to the plasma axis leads to larger acceleration of fluid elements in this direction. The effect is to push the blast wave faster normal to the plasma axis until pressure gradients in all directions become uniform and a nearly spherical blast wave propagates into the domain. Figure 21b shows that as the blast wave propagates to a radius 2 to 3 times the initial size of the plasma it becomes more and more spherical in shape.
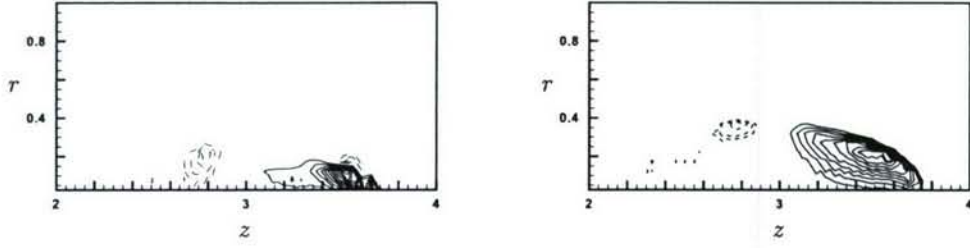
29

Figure 23: Contours of $\hat{\phi}$ component of vorticity at $t = 0.02$ and 0.08, ——— : positive vorticity, ---- : negative vorticity.

3.2.3 Short time behavior

An important feature of the tear–drop shaped idealization is generation of baro-clinic vorticity near the leading and trailing edges of the plasma for times less than 5 μs. Shock waves with varying strength and curvature generate vorticity in the flow (Truesdell 1952, Lighthill 1957, Hayes 1957, Berndt 1966, Kevlahan 1997). A general expression for vorticity jump across an unsteady curved shock propagating into a two–dimensional non–uniform flow was derived by Kevlahan (1997). However a simpler expression for vorticity jump suggested by Truesdell (1952) has been used to explain generation of vorticity near the leading and trailing edges of the plasma. Truesdell considered vorticity jump across a two dimensional steady shock in uniform flow. The jump in vorticity was given by

$$\delta\omega = \frac{\mu^2}{1+\mu}\kappa U_t, \qquad (45)$$

where κ is the curvature of the shock wave, U_t is the velocity tangential to the shock in the frame of reference of the shock wave, and μ is the shock strength given by

$$\mu = \frac{\rho_s}{\rho_\infty} - 1, \qquad (46)$$

where ρ_s and ρ_∞ are the densities at the shock front, and ahead of it respectively. Note that vorticity has been considered to be positive, out of the plane of the paper.

Figure 22a shows a schematic for propagation of a tear–drop shaped shock wave. Note that both curvature and strength of the shock wave varies along its surface. Figure 22b shows the variation of shock strength, shock curvature, tangential velocity and jump in vorticity as a function of z at $t = 0.08$. The curvature of the shock wave is zero near the center and obtains large negative values near the edges of the plasma. The shock strength on the other hand is maximum near the center and decreases towards the edges. The tangential velocity is negative and positive near the leading and trailing edges. The jump in vorticity as obtained
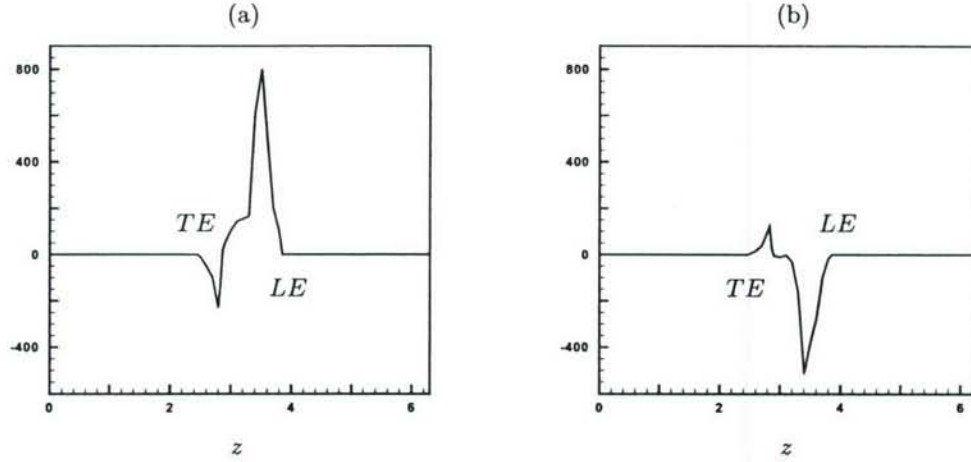
30

Figure 24: (a) Baroclinic term as a function of z at $r = 0.172$ and at $t = 0.02$, (b) Bulk dilatation term as a function of z at $r = 0.172$ and at $t = 0.02$, LE and TE denote leading and trailing edges of the plasma.

from equation 45, is hence found to be positive and negative near the leading and trailing edges of the plasma, respectively.

The vorticity equation for a compressible, viscous flow with variable fluid properties can be written as

$$
\frac{d\vec{\omega}}{dt} = \underbrace{(\vec{u} \cdot \nabla)\vec{\omega}}_{\text{convection}} + \underbrace{(\vec{\omega} \cdot \nabla)\vec{u}}_{\text{vortex stretching/tilting}} - \underbrace{\vec{\omega}(\nabla \cdot \vec{u})}_{\text{bulk dilatation}}
$$

$$
- \underbrace{\frac{\nabla p \times \nabla \rho}{\rho^2}}_{\text{baroclinic}} + \frac{1}{Re}\underbrace{(\nabla \times (\frac{1}{\rho}\nabla \cdot \tau))}_{\text{viscous}} \quad (47)
$$

Since baroclinic vorticity is the only source term in equation 47, it is the only term responsible for initial generation of vorticity in the flow. Note that the flow is axisymmetric. Defining a cylindrical coordinate system along $\hat{r}$, $\hat{\phi}$ and $\hat{z}$ (figure 22a), any gradients in the flow will occur only along $\hat{r}$ and $\hat{z}$ directions. Thus the only possible component of baroclinic vorticity in the flow will be along $\hat{\phi}$.

Figure 23 shows contours of the $\hat{\phi}$ component of vorticity at subsequent instants of time. The contours are shown in a plane passing through the axis of the plasma. Positive and negative vorticity is observed near the leading and trailing edges of the plasma. Vorticity generation is stronger near the leading edge. The magnitude of vorticity is observed to decrease in time, as it spreads out further from the core of the plasma.

Budgets were computed for the different terms on the right hand side of the
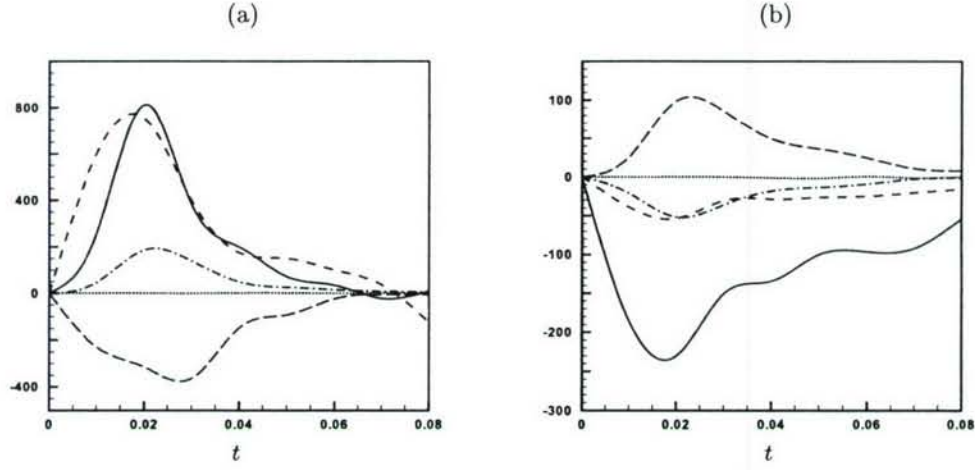
31

Figure 25: (a) Vorticity budget at a point near the leading edge of the plasma ($z = 3.5$, $r = 0.172$), (b) Vorticity budget at point near the trailing edge ($z = 2.8$, $r = 0.172$). $----$: convection, $---$: vortex stretching/tilting , $---$: bulk dilatation, $\longrightarrow$: baroclinic, $\cdots\cdots$: viscous.

vorticity equation and their behavior in time was observed. Figure 24a shows the baroclinic source term as a function of z at $r = 0.172$ and at $t = 0.02$. Positive and negative regions of baroclinic vorticity are observed near the leading and trailing edges of the plasma respectively. The region with positive vorticity is stronger compared to that with negative vorticity. This is because density is lower near the leading edge of the plasma. Also the curvature of the blast wave changes rapidly near the leading edge causing maximum misalignment between the pressure and density gradients. Note that from symmetry considerations, the alignment of ∇p and $\nabla \rho$ near the trailing edge is just the opposite to that near the leading edge. So the baroclinic source term is opposite in sign near the leading and trailing edges of the plasma. Figure 24b shows the bulk dilatation term as a function of z at $r = 0.172$ at the same instant of time. Since there is expansion behind the blast wave ($\nabla \cdot \vec{u}$) is positive. Since vorticity is positive and negative near the leading and trailing edges of the plasma (figure 23), the bulk dilatation term is negative and positive near the leading and trailing edges respectively.

Figure 25 shows time variation of the different terms on the right hand side of the vorticity equation. Near the leading edge of the plasma (figure 25a), the generation of baroclinic vorticity is positive. This generation of vorticity is suppressed in time through the bulk dilatation term which is negative near the leading edge of the plasma. The reverse occurs near the trailing edge (figure 25b) where the alignment of net pressure and density gradients is such that the baroclinic vorticity generated is negative. The bulk dilatation term is positive near the trailing edge and in time counter balances the baroclinic generation of

32

Figure 26: Temperature contours at $t = 18$ μs, 30 μs and 60 μs show breaking and roll up of the temperature field.

vorticity.

Vorticity is observed to be convected in the direction of propagation of the tear-drop shaped blast wave. Thus the spread of vorticity away from the plasma axis (figure 23) can be attributed to the combined effects of vorticity convection and propagation of the blast wave resulting in vorticity generation at locations further from the axis of the plasma. The vortex stretching/tilting term is found to be positive and negative near the leading and trailing edges respectively. The viscous term is 2 to 3 orders of magnitude smaller than any of the other terms and so does not have a significant contribution in the evolution of vorticity in the flow. So, vorticity generated by baroclinic means due to interaction of the curved blast wave with the flow upstream, is convected radially outward, and suppressed by bulk expansion in the core of the plasma.

3.2.4   Long time behavior

This section shows evolution of the core of the plasma at times longer than 5 μs. Experiments in laser–induced break down (Adelgren 2001, Yan 2003) show that the core of the plasma eventually roll up generating a toroidal vortex ring. The time scale for this roll up depends on the amount of laser energy deposited in the flow. Experimental temperature measurements indicate that as a consequence of the roll up, the temperature field is advected such that the peak temperature shifts from the plasma axis to the center of the generated vortex ring.

Figure 26 shows long time evolution of the temperature field obtained in the simulations. Note that the temperature field starts breaking around $t = 18$ μs (figure 26a). The break up starts from the region of maximum temperature along the axis of the plasma. This propagates along the axis of the plasma from
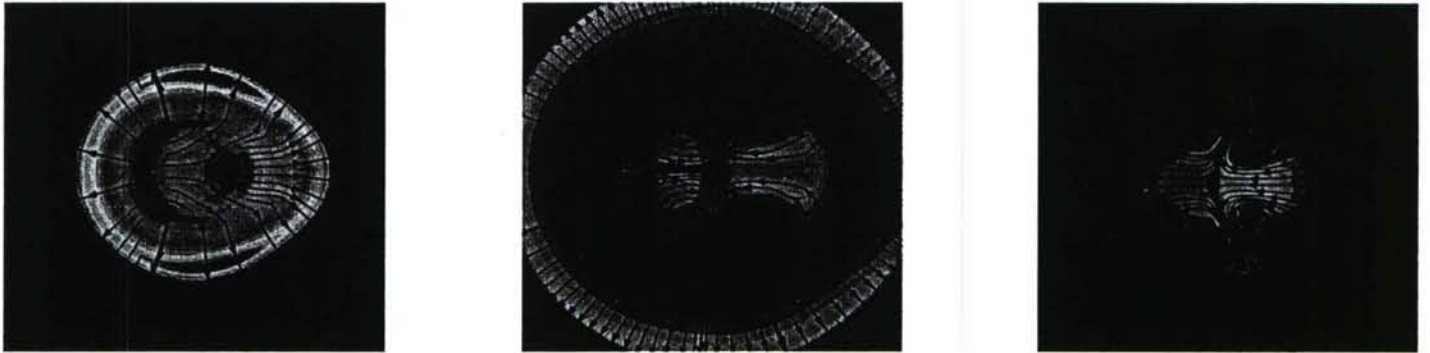
33

Figure 27: Velocity streamlines at $t = 4 \mu s$, $12 \mu s$ and $30 \mu s$.
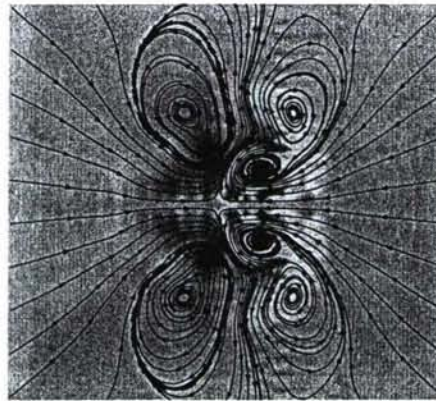

Figure 28: Velocity streamlines plotted over contours of vorticity magnitude at $30 \mu s$.
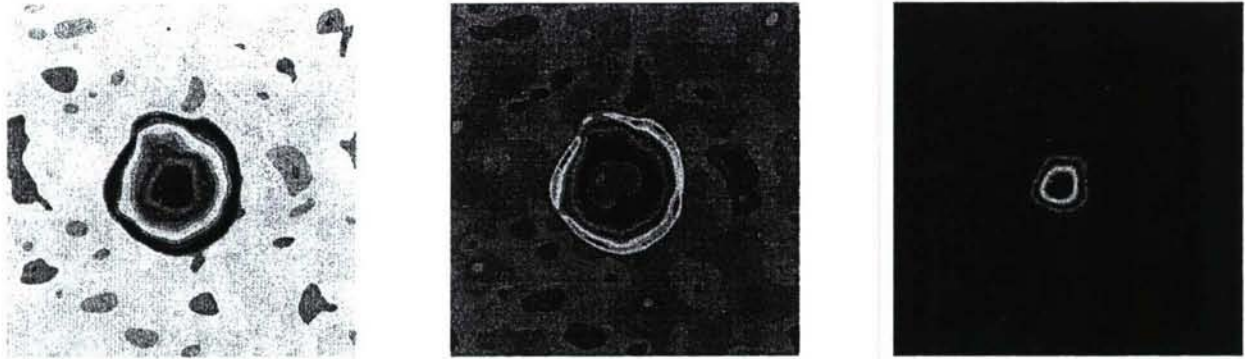
34

Figure 29: Contours of density, pressure and temperature at a given instant of time shows interaction of the spherical plasma with a turbulent background.

right to left resulting in formation of an axisymmetric temperature lobe around 30 μs (figure 26b). In time this temperature lobe moves further away from the plasma axis and finally rolls up to form a toroidal vortex ring as shown in the contours of temperature at 60 μs (figure 26c). Note that during this process, the maximum temperature is advected from the plasma axis to the center of the vortex ring.

The breaking and roll up of the temperature field can be explained by evolution of the velocity field in the core of the plasma. Figure 27 shows time evolution of the velocity field. Initially the core of the plasma expands. This is observed from velocity streamlines moving away from the plasma core (figure 27a). As the blast wave propagates away from the core, it can be shown, from conservation of mass that part of the fluid from the shock front moves back towards the plasma core. Thus a separating streamline is formed, ahead of which the fluid elements move away from the plasma core, but behind which a reverse flow is observed (figure 27b). The reverse flow is strongest along the plasma axis from right to left. Thus two jets of different velocity impinge head on along the plasma axis, yielding a complicated vorticity field (figure 27c). The fact that fluid rushes in from right to left along the plasma axis and then rolls over in a direction normal to the plasma axis leads to breaking and roll up of the temperature field.

Note that the actual vorticity field is much more complicated than just a single toroidal vortex ring. However the magnitude of vorticity is much stronger in the vortex ring closest to the plasma axis. This can be shown by plotting velocity streamlines over contours of vorticity magnitude (figure 28). Thus only a single toroidal vortex ring is observed in the experimental flow visualization.
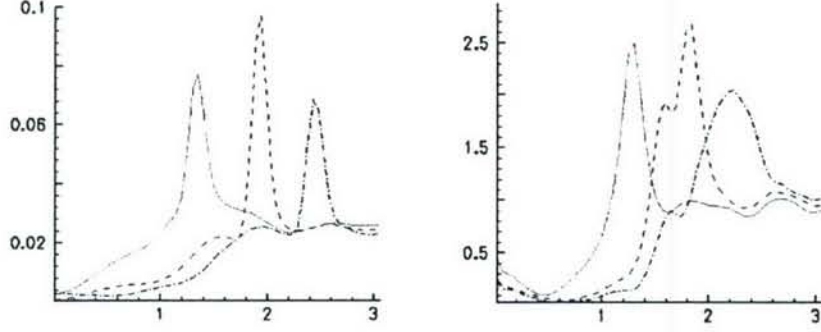
35

Figure 30: Statistics for the radial component of velocity and transverse component of vorticity at three different instants of time.

3.3 Spherical plasma interacting with isotropic turbulence

Direct numerical simulation of isotropic turbulence was performed under conditions corresponding to past DNS by Blaisdell et al. (1991). The initial velocity fluctuations are isotropic and divergence–free, while initial fluctuations in pressure, temperature and density are assumed to be zero. The initial velocity fluctuations are generated using Rogallo's (1981) method. The Fourier coefficients of the initial velocity fields are given by

$$\hat{u} = \frac{\alpha k k_2 + \beta k_1 k_3}{k(k_1{}^2 + k_2{}^2)^{1/2}} e_1 + \frac{\beta k_2 k_3 - \alpha k k_1}{k(k_1{}^2 + k_2{}^2)^{1/2}} e_2 - \frac{\beta(k_1{}^2 + k_2{}^2)^{1/2}}{k} e_3 \qquad (48)$$

where

$$\alpha(k) = \frac{E(k)^{1/2}}{4\pi k^2} e^{i\theta_1} \cos(\phi), \quad \beta(k) = \frac{E(k)^{1/2}}{4\pi k^2} e^{i\theta_2} \cos(\phi). \qquad (49)$$

Here θ_1, θ_2 and ϕ are random numbers from 0 to 2π, and e_i denote the unit vectors along the three coordinate directions.

The initial energy spectrum used in the simulations is a power four spectrum peaking at $k_0 = 5$. The initial flow field thus generated has an fluctuation Mach number $M_t = 0.3$ and turbulent Reynolds number $Re_\lambda = 50$. The turbulent field is allowed to decay for some time after which the velocity derivative skewness attains a steady value in the range of -0.3 to -0.4. The plasma is then introduced by increasing the temperature and pressure at constant density.

Figure 29 shows contours of density, pressure and temperature at a later instant of time. A spherically symmetric blast wave is observed to propagate through the background turbulence compressing the flow in a spherically symmetric manner. There is significant expansion in the plasma core. As the blast wave
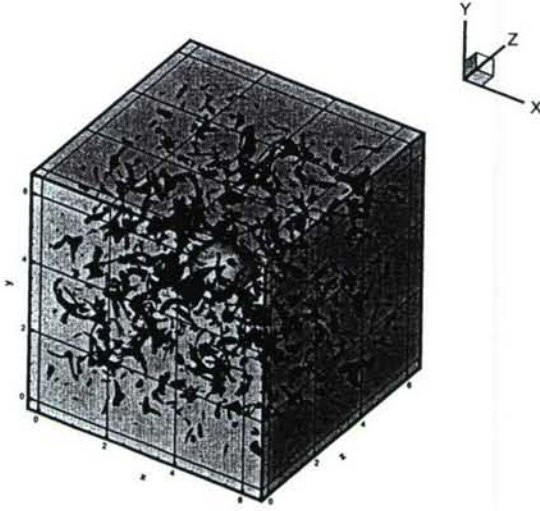
36

Figure 31: Instantaneous isosurfaces of velocity magnitude showing propagation of a blast wave through isotropic turbulence.

propagates significantly into the background, it is observed to get distorted rapidly due to interaction with the turbulence.

Since the problem has radial symmetry, statistics were obtained in a radially symmetric manner. Figure 30 shows statistics for the radial component of velocity and the transverse component of vorticity at three different instants of time. Amplification of turbulence levels are observed in the vicinity of the blast wave. The local compression across the blast wave causes the turbulence levels to amplify. Also since the blast wave is radially symmetric the amplification is most pronounced in the radial component of the velocity and hence in the transverse component of the vorticity.

3.4   Tear–drop shaped plasma interacting with isotropic turbulence

Laser energy is added to this flow by locally increasing the temperature and pressure at constant density. Figure 31 shows a schematic for the problem. Isosurfaces of velocity magnitude has been shown at a given instant of time. A tear–drop shaped blast wave is observed to propagate through the background turbulence. Interaction of this blast wave with the background turbulence and the effect of expansion in the plasma core has been described in this section.

Figure 32 shows propagation of the blast wave through background turbulence. Both side and sectional views have been shown for contours of density plotted at a given instant of time. A very strong blast wave is observed to propagate

37

Figure 32: Contours of density at $t = 2.75$ μs showing propagation of a strong blast wave through the background turbulence.
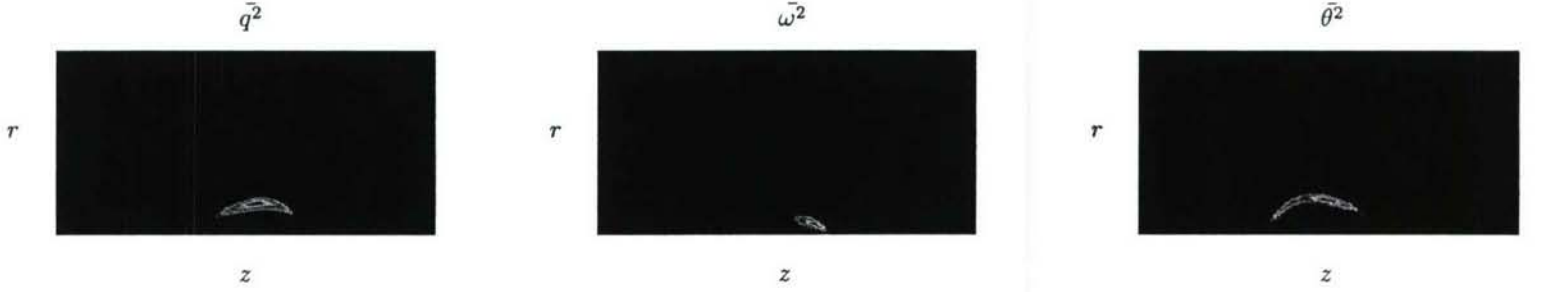

Figure 33: Statistics for turbulent kinetic energy, vorticity and divergence at $t = 1.9$ μs.

into the background compressing the turbulence, leaving the flow in the core to expand. The blast wave is initially strong and hence retains its tear drop shape. But the effect of the background turbulence is to dampen the blast wave intensity and soon it becomes weak enough to interact heavily with the turbulence and its shape gets distorted.

Compression across the blast wave and expansion in the plasma core affect turbulence levels in these regions. Note that the turbulence is statistically homogeneous in axisymmetric planes with respect to the plasma axis. Statistics were therefore computed in $z - r$ planes. Figure 33 shows statistics for turbulent kinetic energy, vorticity and divergence at $t = 1.9$ μs. Note that in the vicinity of the blast wave turbulence levels get amplified due to presence of compression there. This trend is supported by linear analysis of turbulence interacting with
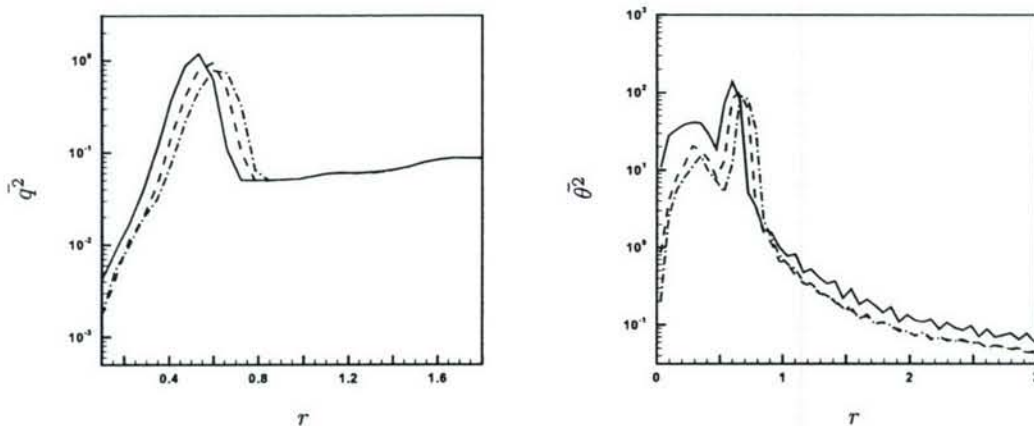
38

Figure 34: Statistics for turbulent kinetic energy and divergence at $t = 1.9 \ \mu s$, $2.25 \ \mu s$ and $2.5 \ \mu s$.

a shock wave (Mahesh et al. 1995,1997). Also the expansion in the plasma core leads to suppression of turbulence levels there. Increase in viscosity due to high temperatures in the core also add to suppression of turbulence levels.

The extent of turbulence amplification across a shock wave would depend on the strength of the shock wave. Thus the extent of amplification should decrease in time as the shock wave propagates into the background with decreasing intensity. Figure 34a shows statistics for turbulent kinetic energy at $t = 1.9 \ \mu s$, $2.25 \ \mu s$ and $2.5 \ \mu s$ plotted as a function of r at z corresponding to the center of the plasma. Note that the turbulence levels get suppressed in the plasma core. Also note that the amplification in turbulence levels across the shock wave decreases in time due to decreasing intensity of the shock wave. Figure 34b shows statistics for divergence in time. The two successive peaks indicate expansion in the core followed by compression across the blast wave. Note that at any given instant of time the effect of compression on the background turbulence is much more pronounced compared to the effect of expansion in the plasma core.

4   Summary

This work uses direct numerical simulation to study the thermal effect of a region of plasma on quiescent air. The simulations solve the compressible ideal gas Navier–Stokes equations using Fourier spectral methods. A shock capturing scheme is incorporated to account for the strong shock waves. Also, a logarithmic formulation for the continuity equation is developed to handle low densities at the core of the plasma.

Two idealizations of the plasma have been considered – spherical and tear–drop shaped. The spherical idealization can be compared to classical solution for
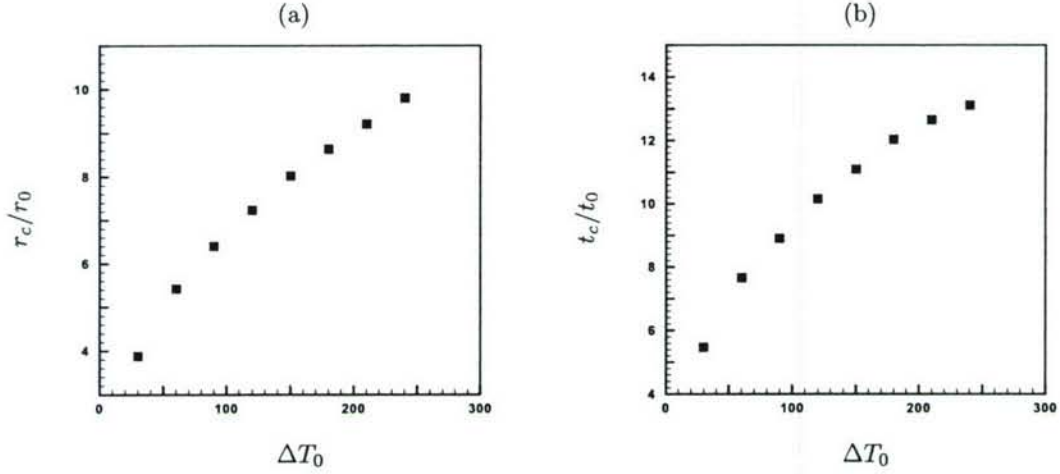
39

Figure 35: (a) Radial location of blast wave corresponding to $M_s = 1.05$ for different ΔT_0, (b) Time required for M_s to reduce to 1.05 for different ΔT_0.

strong shock conditions. The post energy deposition process can be divided into shock formation and propagation phases. During shock formation, large pressure gradients accelerate the flow in the radial direction. This results in the formation of a shock wave whose intensity increases in time until it reaches a maximum. The shock wave then propagates radially, its strength decreasing as a result. Density in the core of the plasma decreases while the shock forms and increases when the shock propagates radially. This behavior of density is explained by conservation of mass. The shock radius and velocity at the shock front are compared to strong shock solutions and are observed to compare well during initial times but later deviate towards the acoustic limit.

The tear–drop shaped idealization resembles the initial shape of the plasma as observed in experiments. Shock radius and jumps in fluid properties at the shock front normal to the axis of the plasma compare reasonably to results from experiments and other simulations. A tear–drop shaped blast wave propagates down the domain, becoming increasingly spherical in time. The pressure gradients are observed to be most intense normal to the axis of the plasma. Also propagation of a curved shock wave through the domain is found to misalign the density and pressure gradients, which generates baroclinic vorticity in the flow. Budgets for the vorticity transport equation show that vorticity generated initially through baroclinic means eventually decreases through bulk expansion in the flow.

For control applications, it is useful to estimate the extent to which the energy addition affects the flow. The blast wave that is generated as a result of energy deposition, decays in intensity until eventually it becomes an acoustic wave. In order to estimate the spatial extent to which the blast wave affects the background flow, we (arbitrarily) define a cut-off value of $M_s = 1.05$. Beyond this

40

M_s the effect of the blast wave is considered small. Figure 35a shows the radial location of the blast wave when M_s decays to its cut-off value, for different ΔT_0. The location of the blast wave r_c is normalized with respect to the initial size of the plasma $r_0 = \pi/20$. The time required to reach this location t_c is shown in figure 35b. t_c is normalized with respect to t_0 which is the time required by an acoustic wave in the background medium to travel a distance equal to the initial size of the plasma. These results are for the spherical idealization of the plasma. Note that when ΔT_0 varies from 30 to 240, r_c/r_0 varies from 3.88 to 9.8 while t_c/t_0 varies from 5.52 to 13.11.

References

[1] KNIGHT, D., KUCHINSKIY, V., KURANOV, A. & SHEIKIN, E. 2003 Survey of aerodynamic flow control at high speed by energy deposition. *AIAA paper 2003-0525.*

[2] ADELGREN, R. G., YAN, H., ELLIOT, G. S., KNIGHT, D., BEUTNER, T. J., ZHELTOVODOV, A., IVANOV, M. & KHOTYANOVSKY, D. 2003 Localized flow control by laser energy deposition applied to Edney IV shock impingement and intersecting shocks. *AIAA paper 2003-31.*

[3] SHNEYDER, M. N., MACHERET, S. O., ZAIDI, S. H., GIRGIS, I. G., RAIZER, YU. P., & MILES, R. B. 2003 Steady and unsteady supersonic flow control with energy addition. *AIAA paper 2003-3862.*

[4] MAKER, P., TERHUNE, R. & SAVAGE, C. 1963 *Proceedings of the Third International Quantum Mechanics Conference*, Paris.

[5] DAMON, E. & TOMLINSON, R. 1963 Observation of ionization of gases by a ruby laser. *Applied Optics* **2(5)**.

[6] MEYERAND, R. & HAUGHT, A. 1963 Gas breakdown at optical frequencies. *Phys. Rev. Let.* **11(9)**, 401–403.

[7] RAIZER, YU. P. 1997 *Gas discharge physics*, 2nd edition, Springer–Verlag, New York.

[8] JIANG, Z., TAKAYAMA, K., MOOSAD, K. P. B., ONODERA, O. & SUN, M. 1998 Numerical and experimental study of a micro-blast wave generated by pulsed laser beam focusing *Shock waves* **8:**, 337–349.

[9] LEWIS, J., PARIGGER, C., HORNKOHL, J., & GUAN, G. 1999 Laser–induced optical breakdown plasma spectra and analysis by use of the program NEQAIR *AIAA paper 99-0723.*

[10] DORS, I., PARIGGER, C. & LEWIS, J. 2000 Fluid dynamic effects following laser–induced optical breakdown *AIAA paper 2000-0717.*

[11] ADELGREN, R., BOGUSZKO, M. & ELLIOTT, G. 2001 Experimental summary report–shock propagation measurements for Nd:YAG laser induced breakdown in quiescent air, Department of Mechanical and Aerospace Engineering, Rutgers University

[12] YAN, H., ADELGREN, M., BOUSZKO, M., ELLIOTT, G.& KNIGHT, D. 2003 Laser energy deposition in quiescent air *AIAA paper 2003-1051.*

[13] TAYLOR, G. I. 1950 The formation of a blast wave by a very intense explosion: I. theoretical discussion. *Proc. Roy. Soc.* **201**, 159–174.

[14] SEDOV, L. I. 1958 *Similarity and dimensional methods in mechanics,* Academic, New York.

[15] VON NEUMANN, J. 1963 The point source solution. *Collected works of J von Neumann, Vol. VI,* Pergamon, England.

[16] BRODE, H. L. 1955 Numerical solution of blast waves. *J. Appl. Phys.* **26(6)**, 766–775.

[17] STEINER, H., GRETLER, W. & HIRSCHLER, T. Numerical solution for spherical laser–driven shock waves. *Shock waves* **8**, 337–349.

[18] KANDALA, R., & CANDLER, G. 2002 Computational modeling of localized laser energy deposition in quiescent air. *AIAA paper 2002-2160.*

[19] ROGALLO, R. S. 1981 Numerical experiments in homogeneous turbulence. *NASA Tech. Memo.* 81315.

[20] BLAISDELL, G. A., MANSOUR, N. N., & REYNOLDS, W. C. 1991 Numerical simulations of compressible homogeneous turbulence., Report No TF-50, Thermosciences Division, Department of Mechanical Engineering, Stanford University.

[21] TRUESDELL, C. 1952 On curved shocks in steady plane flow of an ideal fluid. *J. Aeronaut. Sci.* **19**, 826–828.

[22] KEVLAHAN, N. K. R. 1997 The vorticity jump across a shock wave in a non–uniform flow. *J. Fluid Mech.* **341**, 371–384.

[23] PHUOC, T. X. 2000 Laser spark ignition: Experimental determination of laser–induced breakdown thresholds of combustion gases. *Optics Communications* **175(4)**, 419–423.

[24] MOLINA-MORALES, P., TOYODA, K., KOMURASAKI, K. & ARAKAWA, Y. 2001 CFD simulation of a 2–kW class laser thruster. *AIAA paper 2001–0650.*

[25] WANG, T. S., CHEN, Y.S., LIU, J., MYRABO, L. N. & MEAD, F.B. 2001 Advanced performance modeling of experimental laser lightcrafts. *AIAA paper 2001–0648.*

[26] KANDALA, R., & CANDLER, G. 2003 Numerical studies of laser–induced energy deposition for supersonic flow control. *AIAA paper 2003–1052.*

[27] KANDALA, R., CANDLER, G., GLUMAC, N. & ELLIOTT, G. 2005 Simulation of laser–induced plasma experiments for supersonic flow control. *AIAA paper 2005–0205.*

[28] LEE, J. H. 2005 Electron–impact vibrational relaxation in high temperature Nitrogen. *AIAA paper 1992–0807.*

[29] RAIZER, Y. P 1966 Breakdown and heating of gases under the influence of a laser beam. *Soviet Physics USPEKHI* **8(5)**, 650–673.

[30] RIGGINS, D. W., NELSON, H. F. & JOHNSON, E. 1999 Blunt-body wave drag reduction using focused energy deposition. *AIAA J.* **37(4)**, 460–467.

[31] CANDLER, G. & KELLY, J. 1999 Effect of internal energy on supersonic drag. *AIAA paper 1999–4964.*

[32] CANDLER, G. & KELLY, J. 1996 Shock wave dispersion in nonequilibrium plasma. *AIAA paper 1996–4607.*

[33] ROTH, J. R., SHERMAN, D. M., & WILKINSON, S. P. 1998 Boundary layer flow control with one atmosphere uniform glow discharge surface plasma. *AIAA paper 1998–0328.*

[34] SOLOVIEV, V., KRIVTSOV, V., KONCHAKOV, A. & MALMUTH, N. 1999 Mechanisms of shock wave dispersion and attenuation in weakly ionized cold discharge plasmas. *AIAA paper 1999–4908.*

[35] WHITE, A. R., ESSENHIGH, K.A., ADAMOVICH, I., LEMPERT, W. & SUBRAMANIUM, V. V. 1999 Effects of thermal gradients and ionization on the propagation of spark–generated shock waves. *AIAA paper 1999–4855.*

[36] FERNANDEZ, E., CAPPELLI, M. & MAHESH, K. 1998 Two dimensional simulations of hall thrusters. *Annual Research Briefs-1998*, Center for Turbulence Research, Stanford University, 143–149.

[37] MAHESH, K., LELE, S. K., & MOIN, P. 1995 The interaction of an isotropic field of acoustic waves with a shock wave. *J. Fluid Mech.* **300**, 383–407.

[38] MAHESH, K., LELE, S. K., & MOIN, P. 1997 The influence of entropy fluctuations on the interaction of turbulence with a shock wave. *J. Fluid Mech.* **334**, 353–379.

[39] YEE, H. C., SANDHAM, N. D., DJOMEHRI, M.J. 1999 Low–dissipative high–order shock–capturing methods using characteristic-based filter. *J. Comput. Phys.* **150**, 199–238.

[40] HARTEN, A. 1978 The artificial compression method for computation of shocks and contact discontinuities. *Math. Comp.* **32**, 363.

[41] YEE, H.C. & SHINN, J. 1989 Semi–implicit and fully implicit shock–capturing methods for hyperbolic conservation laws with stiff source terms. *AIAA J.* **27**, 299.

[42] YOUNG, V.Y.C. & YEE, H.C. 1987 Numerical simulation of shock wave diffraction by TVD schemes. *AIAA paper 1987-0112.*

[43] ROHDE, A. 2001 Eigen values and eigen vectors of the Euler equations in general geometries. *AIAA paper 2001-2609.*

[44] DORS, I.G. & PARIGGER, C.G. 2003 Computational fluid–dynamic model of laser induced breakdown in air . *Applied Optics.* **42(30)**.

[45] ROOT, R.G. 1989 Modeling of post–breakdown phenomenon in laser–induced plasma and applications. *Marcel Dekker, Inc., New York* **2** 69–103.

[46] GREY MORGAN, C. 1975 Laser–induced breakdown of gases. *Rep. Prog. Phys.* **38** 621–665.

[47] HAYES, W.D. 1957 The vorticity jump across a gasdynamic discontinuity. *J. Fluid Mech.* **2**, 595–600.

[48] LIGHTHILL, M.J. 1957 Dynamics of a dissociating gas. *J. Fluid Mech.* **2**, 1–32.

[49] BERNDT, S.B. 1966 The vorticity jump across a flow discontinuity. *J. Fluid Mech.* **26**, 433–436.

[50] KEVLAHAN, N.K.R. 1996 The propagation of weak shocks in non–uniform flows. *J. Fluid Mech.* **327**, 161–197.

5 Appendix : Eigen vector Matrix formulation for a generalized coordinate system

Let the Euler equations in conservative form be represented by

$$\frac{\partial \bar{U}}{\partial t} + \nabla \cdot \bar{F} = 0 \tag{50}$$

$\bar{U}$ is the vector of the conserved variables

$$\bar{\mathbf{U}} = \begin{pmatrix} \rho \\ \rho u \\ \rho v \\ \rho w \\ \rho e_0 \end{pmatrix}$$

$\bar{F}$ is the flux vector given by

$$\bar{\mathbf{F}} = \begin{pmatrix} \rho v_n \\ \rho u v_n + p n_x \\ \rho v v_n + p n_y \\ \rho w v_n + p n_z \\ \rho h_0 v_n \end{pmatrix}$$

where

$$v_n = u n_x + v n_y + w n_z \tag{51}$$

And

$$n_x{}^2 + n_y{}^2 + n_z{}^2 = 1 \tag{52}$$

And h_0 is the total enthalpy given by

$$h_0 = h + e_k. \tag{53}$$

Where h is enthalpy and is given by

$$h = e + p/\rho. \tag{54}$$

Let the equation of state for the gas be given by

$$p = \rho R(T)T. \tag{55}$$

Then the elemental change in pressure dp can be written as

$$dp = RT d\rho + \rho \left(R + T\frac{dR}{dT} \right) dT \tag{56}$$

Now since $e = e(T)$ only

$$dT = \left(\frac{dT}{de} \right) de \tag{57}$$

45

Where the internal energy e can be written in terms of the conservative variables u_i. Using the above relations the generalized Jacobian matrix can be computed as

$$
\mathbf{J} = \begin{pmatrix}
0 & 1 & 0 & 0 & 0 \\
(-uv_n + (RT - A(e - e_k))n_x) & (un_x + v_n - Aun_x) & (un_y - Avn_x) & (un_z - Awn_x) & An_x \\
(-vv_n + (RT - A(e - e_k))n_y) & (vn_x - Aun_y) & (vn_y + v_n - Avn_y) & (vn_z - Awn_y) & An_y \\
(-wv_n + (RT - A(e - e_k))n_z) & (wn_x - Aun_z) & (wn_y - Avn_z) & (wn_z + v_n - Awn_z) & An_z \\
(-e_0 v_n - Av_n(e - e_k)) & (e_0 n_x + RT n_x - v_n Au) & (e_0 n_y + RT n_y - v_n Av) & (e_0 n_z + RT n_z - v_n Aw) & (v_n(1 + A))
\end{pmatrix}
$$

Where

$$e_0 = e + e_k \tag{58}$$

is the total energy and e_k is the kinetic energy given by

$$e_k = \frac{1}{2}u_i u_i \tag{59}$$

And the factor A is given by

$$A = \left(R + T\frac{dR}{dT}\right)\frac{dT}{de} \tag{60}$$

The generalized eigen values of the above matrix is obtained as :

$$\lambda = \left(\ v_n - c_1,\quad v_n,\quad v_n + c_1,\quad v_n,\quad v_n\ \right)$$

Where the modified speed of sound c_1 is given by

$$c_1 = ((1 + A)RT)^{1/2} \tag{61}$$

Let a new set of variables be defined such that

$$e_1 = \frac{c_1{}^2}{A(A + 1)} \tag{62}$$

And

$$e_2 = e - e_1 \tag{63}$$

Also define $e_k{}^*$ such that

46

$$e_k{}^* = e_k - e_2 \qquad (64)$$

Using these new variables a possible set of the right eigen vector matrices are obtained as

$$\mathbf{R_1} = \begin{pmatrix} 1 & 1 & 1 & 0 & 0 \\ u - c_1 n_x & u & u + c_1 n_x & n_y & -n_z \\ v - c_1 n_y & v & v + c_1 n_y & -n_x & 0 \\ w - c_1 n_z & w & w + c_1 n_z & 0 & n_x \\ (h_0 - c_1 v_n) & e_k{}^* & (h_0 + c_1 v_n) & u n_y - v n_x & w n_x - u n_z \end{pmatrix}$$

$$\mathbf{R_2} = \begin{pmatrix} 1 & 1 & 1 & 0 & 0 \\ u - c_1 n_x & u & u + c_1 n_x & n_y & 0 \\ v - c_1 n_y & v & v + c_1 n_y & -n_x & n_z \\ w - c_1 n_z & w & w + c_1 n_z & 0 & -n_y \\ (h_0 - c_1 v_n) & e_k{}^* & (h_0 + c_1 v_n) & u n_y - v n_x & v n_z - w n_y \end{pmatrix}$$

$$\mathbf{R_3} = \begin{pmatrix} 1 & 1 & 1 & 0 & 0 \\ u - c_1 n_x & u & u + c_1 n_x & -n_z & 0 \\ v - c_1 n_y & v & v + c_1 n_y & 0 & n_z \\ w - c_1 n_z & w & w + c_1 n_z & n_x & -n_y \\ (h_0 - c_1 v_n) & e_k{}^* & (h_0 + c_1 v_n) & w n_x - u n_z & v n_z - w n_y \end{pmatrix}$$

Then the corresponding set of left eigen vector matrices can be obtained as

$$[L] = [R]^{-1} \qquad (65)$$

and they are given by

$$\mathbf{L_1} = \begin{pmatrix} \frac{A e_k{}^* + c_1 v_n}{2 c_1{}^2} & -\frac{A u + c_1 n_x}{2 c_1{}^2} & -\frac{A v + c_1 n_y}{2 c_1{}^2} & -\frac{A w + c_1 n_x}{2 c_1{}^2} & \frac{A}{2 c_1{}^2} \\[2mm] \frac{c_1{}^2 - A e_k{}^*}{c_1{}^2} & \frac{A u}{c_1{}^2} & \frac{A v}{c_1{}^2} & \frac{A w}{c_1{}^2} & -\frac{A}{c_1{}^2} \\[2mm] \frac{A e_k{}^* - c_1 v_n}{2 c_1{}^2} & -\frac{A u - c_1 n_x}{2 c_1{}^2} & -\frac{A v - c_1 n_y}{2 c_1{}^2} & -\frac{A w - c_1 n_x}{2 c_1{}^2} & \frac{A}{2 c_1{}^2} \\[2mm] \frac{v - v_n n_y}{n_x} & n_y & \frac{n_y{}^2 - 1}{n_x} & \frac{n_y n_z}{n_x} & 0 \\[2mm] \frac{v_n n_x - w}{n_x} & -n_z & \frac{-n_y n_z}{n_x} & \frac{1 - n_z{}^2}{n_x} & 0 \end{pmatrix}$$

47

$$\mathbf{L_2} = \begin{pmatrix} \frac{Ae_k{}^{\bullet}+c_1v_n}{2c_1{}^2} & -\frac{Au+c_1n_x}{2c_1{}^2} & -\frac{Av+c_1n_y}{2c_1{}^2} & -\frac{Aw+c_1n_z}{2c_1{}^2} & \frac{A}{2c_1{}^2} \\[2ex] \frac{c_1{}^2-Ae_k{}^{\bullet}}{c_1{}^2} & \frac{Au}{c_1{}^2} & \frac{Av}{c_1{}^2} & \frac{Aw}{c_1{}^2} & -\frac{A}{c_1{}^2} \\[2ex] \frac{Ae_k{}^{\bullet}-c_1v_n}{2c_1{}^2} & -\frac{Au-c_1n_x}{2c_1{}^2} & -\frac{Av-c_1n_y}{2c_1{}^2} & -\frac{Aw-c_1n_z}{2c_1{}^2} & \frac{A}{2c_1{}^2} \\[2ex] \frac{v_nn_x-u}{n_y} & \frac{1-n_x{}^2}{n_y} & -n_x & \frac{-n_xn_z}{n_y} & 0 \\[2ex] \frac{w-v_nn_z}{n_y} & \frac{n_xn_z}{n_y} & n_z & \frac{n_x{}^2-1}{n_y} & 0 \end{pmatrix}$$

$$\mathbf{L_3} = \begin{pmatrix} \frac{Ae_k{}^{\bullet}+c_1v_n}{2c_1{}^2} & -\frac{Au+c_1n_x}{2c_1{}^2} & -\frac{Av+c_1n_y}{2c_1{}^2} & -\frac{Aw+c_1n_z}{2c_1{}^2} & \frac{A}{2c_1{}^2} \\[2ex] \frac{c_1{}^2-Ae_k{}^{\bullet}}{c_1{}^2} & \frac{Au}{c_1{}^2} & \frac{Av}{c_1{}^2} & \frac{Aw}{c_1{}^2} & -\frac{A}{c_1{}^2} \\[2ex] \frac{Ae_k{}^{\bullet}-c_1v_n}{2c_1{}^2} & -\frac{Au-c_1n_x}{2c_1{}^2} & -\frac{Av-c_1n_y}{2c_1{}^2} & -\frac{Aw-c_1n_z}{2c_1{}^2} & \frac{A}{2c_1{}^2} \\[2ex] \frac{u-v_nn_x}{n_z} & \frac{n_x{}^2-1}{n_z} & \frac{n_xn_y}{n_z} & n_x & 0 \\[2ex] \frac{v_nn_y-v}{n_z} & \frac{-n_xn_y}{n_z} & \frac{1-n_y{}^2}{n_z} & -n_y & 0 \end{pmatrix}$$